Newsletters on Stratigraphy, Vol. 55/3 (2022), 333–360 **Article**
Published online November 19, 2021; published in print June 2022

The Messinian on Gavdos (Greece) and the status of currently used ages for the onset of the MSC and gypsum precipitation

Willem Jan Zachariasse[1] and Lucas J. Lourens[1]*

With 9 figures and 2 plates

Abstract. The Upper Tortonian and Messinian in the already classic Metochia section on Gavdos Island (Greece) is made up of deep marine, laminated and homogeneous marls with the latter being replaced by evaporitic limestones at the very top of the section. Previous tuning of the section to the La90 time series of northern summer insolation provided ages for sedimentary cycles, polarity reversals, and bioevents. Earlier work on foraminifers and stable isotopes focused on the last 2.45 Myr of the Tortonian and the first 470 kyr of the Messinian. This study extends the stable isotope record and the set of semi-quantitative data on planktonic foraminifers into the youngest 820 kyr of the section which include the precursor and initial stages of the Messinian Salinity Crisis (MSC). New and old foraminiferal oxygen and carbon isotope data have been combined into a ~25 kyr resolution record for the entire pre-evaporitic Messinian and show a major change at 6.74 ± 0.04 Ma which we interpret to reflect an abrupt change in salinity from normal marine to hypersaline and thus marks the prelude to the MSC. Field and thin-section observations on the limestones in the top of the section confirm their evaporitic origin and suggests that salinities has risen to values of >70 psu. We further discuss the biotic response to the two-step salinity increase during the Messinian. Tuning provides an age of 6.00 Ma for the base of the first evaporitic limestone on Gavdos and this age is therefore the age for the onset of the MSC in this part of the Mediterranean. An evaluation of the published ages for the MSC onset in sections Perales (SE Spain), Monticino (N Italy), and Falconara (Sicily) shows that the onset in Falconara, just as on Gavdos, begins at ~6.00 Ma with calcium carbonate precipitation, whereas in Perales and Monticino, onset begins at 5.97 Ma (similar to the currently used age of 5.971 Ma) with gypsum precipitation, i. e. some 30 kyr later than the onset of the MSC on Gavdos and Sicily (Falconara).

Key words. Messinian Salinity Crisis, Mediterranean, biostratigraphy, stable isotopes, tuning

1. Introduction

The Messinian Salinity Crisis (MSC) refers to a period of ~640 kyr at the end of the Miocene during which the Mediterranean transformed from a normal-marine basin with surface inflow and deep outflow into a salt-saturated basin with restricted exchange and massive salt extraction (materialized in the Lower Evaporites), then into an isolated and desiccated basin, then a brackish water basin and back again to a normal-marine basin at the beginning of the Pliocene.

This prodigious story goes back to the discoveries made by DSDP Leg 13 (Ryan 1973, Ryan et al. 1973, Hsü et al. 1973) and the plethora of research that followed. Debates first focused on controversies such as a deep (2000 m or more) versus shallow desiccated Mediterranean, continuity of marine conditions versus complete or repeated desiccation, and on deep versus

Authors' addresses:
[1] Department of Earth Sciences, Faculty of Geosciences, Utrecht University, Vening Meinesz building A, Princetonlaan 8a, 3584 CB, Utrecht, The Netherlands; w. j.zachariasse@uu.nl; l. j.lourens@uu.nl
* Corresponding author l. j.lourens@uu.nl

www.borntraeger-cramer.de
DOI: 10.1127/nos/2021/0677 0078-0421/2021/0677 $ 7.00

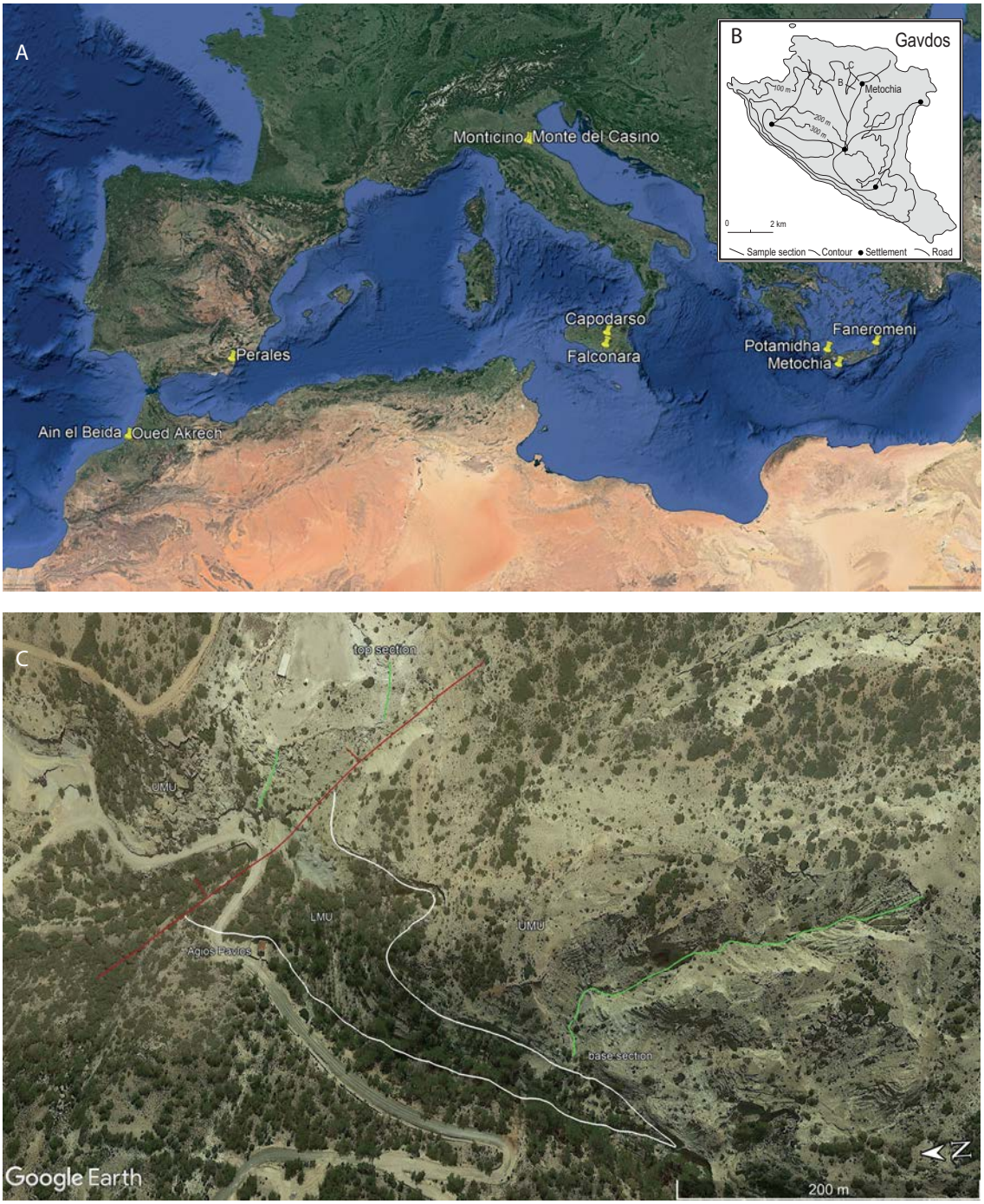

Fig. 1. (A) Location map (Google Earth) of all sections that have been studied (in whole or in part) or mentioned in the text. The Perales section is one of five nearby sections that make up the Abad composite section (see Sierro et al. 2001); (B) Topographic map of Gavdos with location of section Metochia; (C) Detailed satellite map (imagery date 7-1-2017) of the entire Metochia section with subsections sampled on both sides of a 328° NW–148° SE trending normal fault (in red). Subsections are spliced by lithological markers and cycle characteristics. White line represents an erosional unconformity separating an Upper Marine Unit (UMU) with section Metochia from a Lower Marine Unit (LMU).

20220728-121929
A17159/66424/83D369E2

shallow-water (sabkha) origin of the evaporites but later also on questions as glacio-eustatic versus tectonic control of evaporite formation and whether or not desiccation is followed by spill-overs of brackish water from the Black Sea and marine water from the Atlantic between desiccation and Pliocene flooding.

Most of these disputes have been sorted out through studies in uplifted marginal basins that were not much deeper than 1 km (Hilgen et al. 2007, Roveri et al. 2014a) and by modelling studies (Meijer 2006, Meijer 2012, Rohling et al. 2008, Roveri et al. 2014b, Simon and Meijer 2015). As DSDP Leg 13 (and later DSDP Leg 42A) sampled only the upper few tens of meters of Messinian evaporites (probably Upper Evaporites), the full deep basin record of the MSC is known only on seismic images (Lofi et al. 2011a, Lofi et al. 2011b, Lofi 2018) leaving questions on age and nature of evaporite formation in the deepest basins and the fate of these basins during desiccation unanswered albeit that Gvirtzman et al. (2017), Simon and Meijer (2017) and Haq et al. (2020) are beginning to provide some understanding on these points.

Current definition equates the onset of the MSC with the beginning of evaporite formation (Krijgsman et al. 1999a, Hilgen et al. 2007, Manzi et al. 2013). One of the best locations to study the precursor and initial stages of the MSC is the Metochia section on Gavdos (Fig. 1). This section exposes a Middle Tortonian to Messinian sequence of deep marine laminated and homogeneous marls with the latter being replaced by evaporitic limestones in the top part of the section (Krijgsman et al. 1999a).

The 123 meters thick section (described and sampled in November 1991 and June 1992) is tuned to the La90 time series of northern summer insolation by Hilgen et al. (1995) and Krijgsman et al. (1999a) providing an age of 5.98 Ma for the first of five evaporitic limestone beds and thus for the onset of the MSC. Interpretable paleomagnetic and semi-quantitative data on the distribution of age diagnostic planktonic foraminifers are available for the lower 97 meters (Krijgsman et al. 1995, Zachariasse et al. 2011) and the same applies for data on stable isotopes and benthic foraminifers (Seidenkrantz et al. 2000). These lower 97 meters cover the interval of sedimentary cycles M1 to M83 corresponding with the time span between 9.68 and 6.96 Ma (Hilgen et al. 1995).

In this study we extended the stable isotope and microfossil data upward into the uppermost 26 meters of the Metochia section and we made new field and thin-section observations on the limestones. The new and existing data have been combined into an integrated picture for the Messinian on Gavdos with special focus on the manifestation and ages of the precursor and initial stages of the MSC. We further evaluated age and origin of the first limestone in section Falconara (Sicily) and the status of the currently used age for the first gypsum in the Abad section in SE Spain and the Monticino section in N Italy (for locations, see Fig. 1A).

2. An overview of the Messinian succession

The Messinian in section Metochia includes 61 sedimentary cycles of deep marine sediments numbered M73–M133 in Fig. 2. The first 21 cycles (M73–M93) are made up of laminated marls (sapropels) and homogeneous marls whereby base sapropel defines base cycle. The sapropels in the following 35 cycles are partially replaced by laminated marls rich in siliceous microfossils such as radiolarians, diatoms, sponge spicules (termed diatomites and numbered D1–D36 in Fig. 2). The uppermost five cycles consist of laminated marls (mostly diatomites) and limestone beds.

The depositional depth for the pre-diatomite interval is estimated at ~1200 m by Van Hinsbergen and Meulenkamp (2006) using the relationship between % planktonic foraminifers and depth as quantified by Van der Zwaan et al. (1990). If we use the distribution of benthic foraminiferal depth marker species in Seidenkrantz et al. (2000) and depth ranges for these species in Van Hinsbergen et al. (2005) then we arrive at a depositional depth range of roughly 750–1000 m for the pre-diatomite interval. No reliable depth estimates can be made for the interval with diatomites and limestones because of the overall paucity of benthic foraminifers and absence of depth marker species. The lithology, however, does not give any reason to assume that the depth has changed in the diatomite and overlying limestone interval.

The sedimentary cycles in Metochia are the result of precession dominated dry to wet climate oscillations (Hilgen et al. 1995, Schenau et al. 1999) whereby laminated marls formed during the prevalent wet climatic conditions at times of maximum northern summer insolation (for a review on the formation of such cycles in the recent past, see Rohling et al. (2015) and references therein).

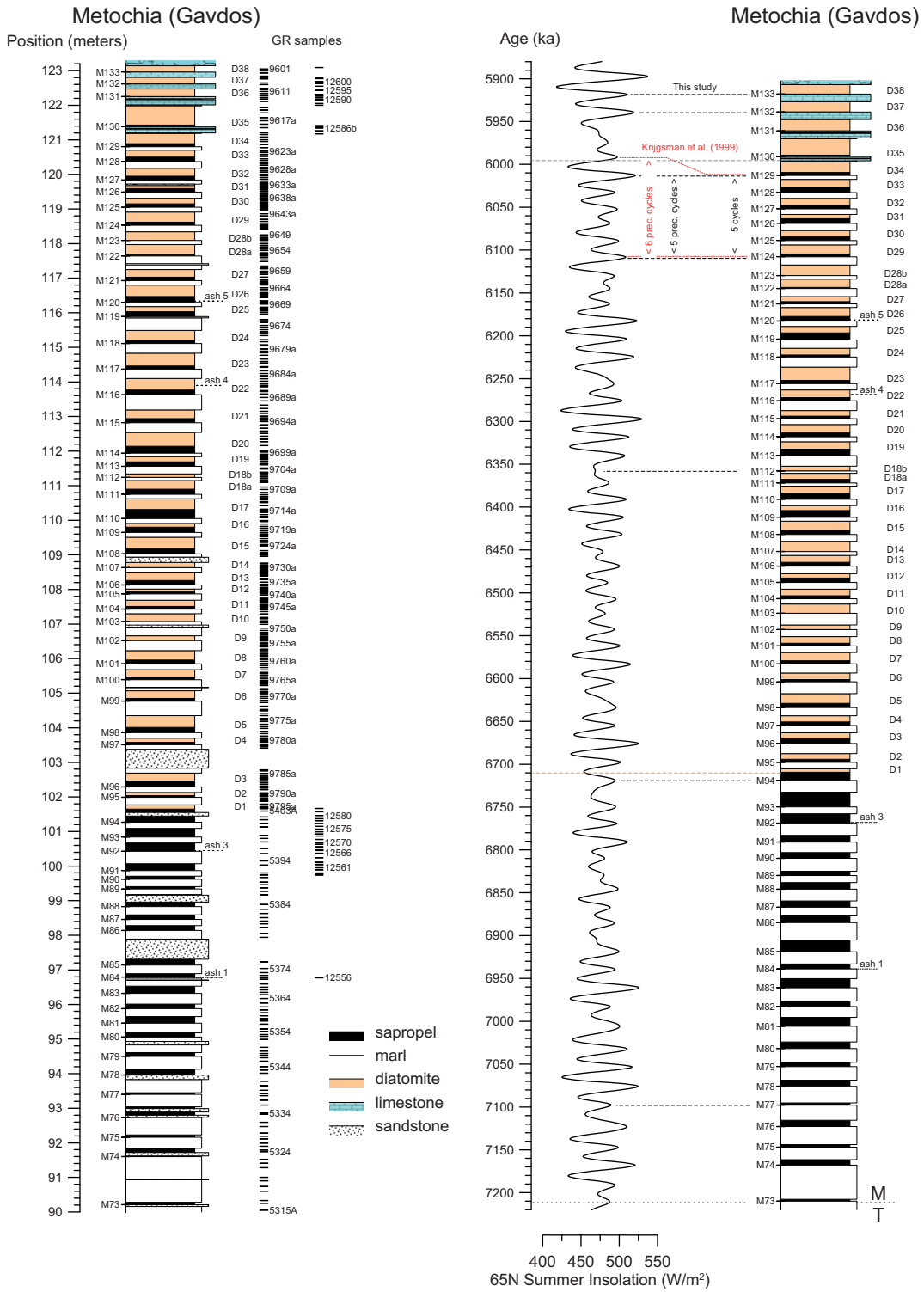

Fig. 2. The Messinian succession of section Metochia after Krijgsman et al. 1995, Krijgsman et al. 1999a and this study (samples GR12557–12603). T/M marks the Tortonian-Messinian boundary. Sedimentary cycles are indicated by M and numbered upwards from the base of the entire section; D numbers refer to diatomite layers. Ash layers occur in cycles M84 and M92 (Hilgen et al. 1997), M116 (field notes Krijgsman et al. 1999a) and a new one at base of cycle M120 (with abundant volcanic glass and some biotite flakes). Ash 2 is absent in Metochia but present in time-equivalent sections on Crete (see Hilgen et al. 1997). The Messinian cycles M73–M133 are tuned to the La2004 time series of northern summer insolation on the right side of the figure. The tuned section is stripped of turbiditic sandstones because they represent instants of time. For the tuning, the base of each cycle is correlated to its inferred insolation maximum, i. e. without a time lag.

20220728-121929
A17159/66424/83D369E2

3. Material and methods

Washed residues (125–600 micron) of new (this study) and old (Krijgsman et al. 1995, Krijgsman et al. 1999a) samples from section Metochia (Fig. 2) were used for the analysis of the planktonic foraminiferal faunas and determination of presence/absence of radiolarians and siliceous sponge spicules.

Residues were further used for measuring stable oxygen and carbon isotopes of benthic and planktonic foraminifers from 10 successive homogeneous marl beds below and from 29 such beds above the first diatomite in cycle M94 using a VG SIRA 24 mass spectrometer. Samples are exclusively from homogeneous beds to minimize the effects of river discharge and low-oxygen deep water conditions on isotope values at times of minimum precession and thus maximize the information on surface and deep water salinity. The new isotope data are combined with the old Messinian isotope data of Seidenkrantz et al. (2000) into a single data set for the entire pre-evaporitic Messinian (see Appendix 1 for all isotope data).

Planktonic foraminiferal species that have been measured are: *Globigerinoides trilobus*, *Globigerinoides obliquus* (may include *Globoturborotalita apertura*), *Globigerina bulloides*, *Globigerina pseudobesa*, and *Orbulina universa*. Measured benthic foraminifers belong to the *Cibicides* species *kullenbergi*, *pseudoungarianus*, *ungarianus* and *wuellerstorfi*, or mixtures thereof but from cycle M94 upwards we had to resort to *Bulimina aculeata* because this is the only benthic species in the homogeneous marls being persistently present in sufficiently large numbers.

Samples of 30–100 specimens per planktonic foraminiferal species and 30–50 specimens per benthic foraminiferal species in the size range of 125–600 micron were first roasted in vacuum and thereafter treated with hydro-phosphoric acid at 100 °C for 90 min, using an ISOCARB common bath preparation device. During each run, up to 17–42 samples were automatically measured in succession including 6–9 in-house (NAXOS) and 2–3 external (IAEA-CO-1) standards and 9–30 individual foraminiferal samples. The standards were placed at the beginning, middle and end of each run to allow for drift correction. After correction, 14 IAEA-CO-1 standards yielded a standard error (95 % confidence limits) of 0.08‰ for $\delta^{13}C$ and 0.12‰ for $\delta^{18}O$. All data are reported as deviations in per mil (‰) to the VPDB standard.

Isotopic offsets between species were calculated using the new data plus the entire (Tortonian and Messinian) data set of Seidenkrantz et al. (2000). All isotope values are calibrated to *C. wuellerstorfi* and *G. obliquus*. By far the most replicate analyses (73) were performed on *C. wuellerstorfi* and mixed *Cibicides* yielding a mean offset of 0.24‰ for $\delta^{13}C$ and 0.08‰ for $\delta^{18}O$. We derived a mean offset between *C. wuellerstorfi* and *B. aculeata* of 1.26‰ for $\delta^{13}C$ and –0.07‰ for $\delta^{18}O$ by combining the individual offsets of five replicate analyses between *B. aculeata* and *C. kullenbergi*, *C. wuellerstorfi*, and mixed *Cibicides*. A complete overview of the offset corrections between species is given in Appendix 2.

Preservation is overall good in the lower part but that of *B. aculeata* in the upper part is variable and defined by three indices: (1) test wall is shiny, (2) dull or (3) dull and granular with category 1 being pristine and 3 slightly recrystallized. Comparison between the preservation state and oxygen and carbon isotopes, however, does not show any significant correlation (see Appendix 3 and 4).

There has been some discussion in the literature on the isotopic fractionation between *C. wuellerstorfi* and ambient seawater. The most commonly used correction factors are those of Shackleton and Opdyke (1973) and Shackleton and Hall (1984) with an offset of 0.64‰ for $\delta^{18}O$ and no offset for $\delta^{13}C$ compared to the ambient seawater isotopic composition. New studies show that deep living *Cibicides* is in close isotopic equilibrium with seawater (Marchitto et al. 2014). If we apply our offset corrections between *B. aculeata* and *C. wuellerstorfi* of 1.26‰ for $\delta^{13}C$ and 0.12‰ for $\delta^{18}O$ (see Appendix 2) then the resulting fractionation factors for *B. aculeata* to ambient seawater fall well within those obtained from culture experiments (McCorkle et al. 2008). Hence we assume that the (corrected) benthic isotope values of *B. aculeata* reflect the changes in the isotopic composition of the deep waters in the EMED fairly well. The same applies for *G. obliquus* because the fractionation between the living descendant of *G. obliquus*, namely *Globigerinoides ruber*, and seawater is small (e. g. Rohling et al. 2004).

4. Results

4.1. The tuning of the pre-evaporitic Messinian succession

The tuning of the Messinian cycles to the La90 northern summer insolation time series by Krijgsman et al.

(1999a) gives ages of 6.72 Ma and 5.98 Ma for the base of the first diatomite cycle M94 and the first limestone in cycle M129. Their tuning is firmly anchored in cycles M111–112 and M122–123. These cycles were first described as single cycles but later interpreted as double cycles because each of their thick diatomaceous beds is interrupted by a layer with vague or absent laminations. These weakly developed homogeneous marl beds have been tied to weak minima in the northern summer insolation time series (see Fig. 1 in Krijgsman et al. 1999a). An alternative tuning to that of Krijgsman et al. (1999a) is presented for the interval above their bioevent 9 in cycle M125 because the first limestone is 4 cycles higher up in the section and thus correlates with the northern summer insolation minimum that precedes the one picked by Krijgsman et al. (1999a) (see Fig. 2). The tuning of the Messinian cycles to the La2004 northern summer insolation time series in this study shows that the age for the onset of diatomite formation remains at 6.72 Ma but the age for the base of the first limestone changed from 5.98 Ma to 6.00 Ma (Fig. 2). The tuning of the interval with limestones is complicated by the eccentricity minimum and interference of obliquity and precession in the northern summer insolation time series and will be discussed in more detail in chapter 4.4.

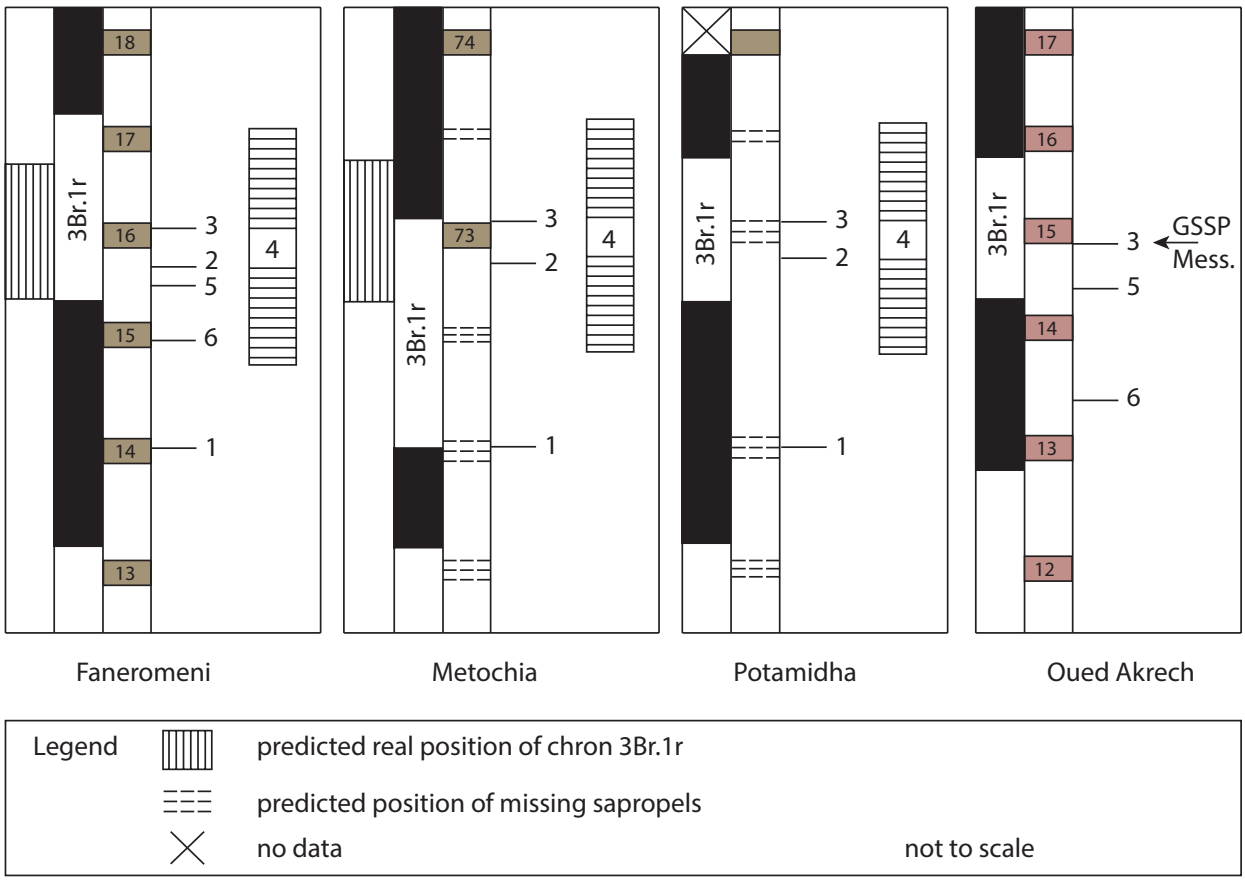

Fig. 3. Correlation between three Cretan T/M boundary sections and the Messinian GSSP section Oued Akrech in Morocco. Reddish clayey marl beds in section Oued Akrech and sapropels in the Cretan sections deposited at times of minimum precession (Hilgen et al. 2000). Sapropel numbers and identified polarity intervals in sections Faneromeni and Metochia after Krijgsman et al (1995). Reddish layer numbers and identified polarity intervals in section Oued Akrech after Hilgen et al. (2000). The magnetobiostratigraphy of section Potamidha is after Langereis (1979) and Zachariasse (1979). Biomagnetostratigraphy is used to align sapropels and reddish layers and to predict sapropel positions in sections Metochia and Potamidha where such layers have not developed. Planktonic foraminiferal bioevents (this study): (1) spike of left-coiled *G. menardii* within the stratigraphic range of dextrally coiled *G. menardii* form 5; (2) LO *G. menardii* form 5; (3) FO *G. miotumida*; (4) absence interval of *G. nepenthes*. Calcareous nannofossils bioevents (Negri and Villa 2000, Hilgen et al. 2000): (5) FO *Amaurolithus delicatus*; (6) FCO *Reticulofenestra rotaria*.

4.2. Position and age of the Tortonian-Messinian (T/M) boundary

The GSSP for the Messinian, defined at the base of cycle OA15 in the Oued Akrech section in Morocco (for location, see Fig. 1A), coincides with the FCO of *Globorotalia miotumida* and falls within the brief reversed Chron 3Br.1r (Hilgen et al. 2000). The base of cycle OA15 in the Messinian GSSP section is equated with the base of sapropel M73 in section Metochia in accordance with the position of this sapropel within Chron 3Br.1r and the FO of *G. miotumida* directly above this sapropel (Hilgen et al. 2000). Fig. 3 shows that sapropel M73 falls in the top part of C3Br.1r but the supposedly time-equivalent reddish layer OA15 is positioned in the middle of this chron. Sapropel 16 in the cyclically-bedded Faneromeni section on E Crete (Krijgsman et al. 1994; for location, see Fig. 1A) occupies the same position within C3Br.1r as OA15 in Oued Akrech but top of chron is younger in Faneromeni than in Oued Akrech (compare positions Faneromeni sapropel 17 and Oued Akrech OA16 in Fig. 3). Top and bottom of C3Br.1r in section Potamidha on W Crete (for location, see Fig. 1A) seems positioned in accordance with top and bottom in section Oued Akrech but unlike the latter is Potamidha not clearly cyclically-bedded (Fig. 3). Our correlation of the three Cretan sections with Oued Akrech shows that the FO of *G. miotumida* on Crete is some 10 kyr younger than its FCO in Morocco. Confirmation of the cyclostratigraphic correlations between Crete and Oued Akrech could have been provided by the presence of bioevents 1 and 4 in section Oued Akrech but we found both absent. The FO of *Amaurolithus delicatus* and FCO *Reticulofenestra rotaria* in section Faneromeni (Negri and Villa 2000) and Oued Akrech (Hilgen et al. 2000), however, seem to confirm the correlations based on planktonic foraminifers and polarity data (Fig. 3).

The missing sapropel in between sapropels M73 and M74 (Fig. 3) has been included in our tuning of section Metochia and provides an age of 7.21 Ma for base M73 and thus for the T/M boundary (Fig. 2). This age is ~36 kyr younger than the current age of 7.246 Ma based on the tuning of section Oued Akrech (7.251 Ma in Hilgen et al. 2000, but revised to 7.246 Ma in Hilgen et al. 2012). The origin of this age discrepancy is unclear but may stem from the tuning of section Oued Akrech.

4.3. The limestones: origin and tuning

An isolated remnant on the Metochia plateau (Plate 1A) exposes the top part of the Metochia section consisting of five limestone beds with laminated marls in between (Plate 1B). The detailed record is shown in Fig. 4 and based on Krijgsman et al. (1999a) and a short revisit in 2003 by the senior author.

The first limestone shows a coarsely mottled appearance with vague and discontinuous planar bedding in the lower 11 cm (Plate 1C). Likely, some of the thicker receding layers are marly. A thin section (GR 12586a in Fig. 4) shows an azoic mottled micritic limestone with vague mm-scale layering and patches with (often) lighter colored rims. The upper 5 cm is finely bedded and a thin section (GR 12586b in Fig. 4) shows irregular mm-scale layers of finely mottled lime mud (Plate 2A).

The coarsely mottled fabric of the lower 11 cm suggests disruption by burrowing but absence of internal details and branching, the blocky outline of some mottles, and the partial preservation of the fine bedding make bioturbation not very likely. The mottles also do not clearly classify as clasts but rather seem to have a diagenetic origin the more so since they are intertwined by spar. The upper 5 cm is turbiditic if the lateral discontinuities in the marly interbeds are caused by scouring. Alternatively, these discontinuities, which also occur in the lower mottled part, may represent load casts (Plate 1C).

The lower 15 cm of the second limestone is massive at the base and becomes finely bedded upwards (Plate 1D). A thin section from the bottom 4 cm (GR 12589) shows a packstone of calcareous ooids with rims of radial crystal fabric and variable thickness (Plate 2B). Co-occurring miliolids are isolated, with or without rims, or enclosed within the ooids. A few supposedly sponge spicules show rims as well. Today, calcareous ooids form in warm and shallow marine (wave-agitated) carbonate environments, some being hypersaline, with a role for microbes to allow carbonate precipitation (Simone 1980, Summons et al. 2013). The ooids and miliolids therefore are transported from shallow water. Since miliolids are known to survive hypersaline conditions as high as 70 psu in the shallow waters of the Red Sea (Murray 1991), the ooids could have formed under hypersaline or even supersaturated conditions. The next 11 cm of the lower part of the second limestone is finely bedded. Thin sections (GR 12589–12590) show mm-scale layers of finely mottled lime mud with a 1 cm thick grainstone

20220728-121929
A17159/66424/83D369E2

Plate 1. (A) Uppermost part of section Metochia; (B) Homogeneous marls (H) of cycles M127 and M128 and first and second limestone of cycles M129 and M130 with intervening diatomites; (C) Close-up of the first limestone; (D) Close-up of the second limestone separated by a marl layer with poorly preserved foraminifers; (E) Slumped limestone bed at the top; (F) Isolated outcrop of laminated marls (with among others epiphytic benthic foraminifers, calcareous nannofossils, marine diatoms and dinoflagellates) in between laminated gypsum beds at the village of Agia Varvara (central Crete); (G) Laminated gypsum at the village of Ploutis (central Crete).

including small sized reworked foraminifers with amongst other orbulinids, *G. bulloides*, bolivinids, miliolids, planispiral and trochospiral benthic specimens in sample GR 12590 (Plate 2C and C1). The source of this turbiditic grainstone is clearly in deeper water than the packstone with ooids. The finely mottled lime mud is intertwined with spar suggesting a diagenetic origin of the mottled texture.

The top of the lower part of the second limestone is irregular and partly wavy and overlain by a thin calcareous marl and limestone (Plate 1D). A thin section (GR 12592) from the 6 cm thick and finely bedded limestone of the upper part of the second limestone (Plate 1D) again shows mm-scale layers of finely mottled lime mud, this time with few minute benthic foraminifers in one of these layers. The 5 cm thick marl in between lower and upper part of the second limestone contains poorly preserved foraminifers.

The third and fourth limestone are finely bedded just as the slumped limestone at the top (Plate 1E). A thin section from the third limestone (GR 12597) shows mm-scale layers of finely mottled lime mud without microfossils (Plate 2D). Again, mottling is probably caused by diagenesis. Bedding in the slumped limestone at the top is largely preserved (Plate 1E) indicating that the limestone derived from a nearby upslope location.

Krijgsman et al. (1999a) interpreted the limestones as evaporitic based on their fine bedding. Our observations show some clear examples of fine/medium grained turbidites in the second limestone and perhaps in the upper part of the first limestone but most limestones are mottled mm-scale layered lime muds in thin sections whereby the intertwining of spar and lime mud points to a diagenetic origin of the mottling. The lime mud with mm-scale layering is a strong argument for an evaporitic origin of the limestones and therefore these limestones replace the homogeneous marl beds of the preceding cycles in accordance with Krijgsman et al. (1999a).

Figure 4 shows that the tuning is straightforward up to the first limestone providing an age of ~ 6.00 Ma for the onset of evaporitic limestone formation on Gavdos. The laminated marl of the next younger cycle M130 is twice as thick as that in the preceding cycles suggesting that laminated marl deposition occurred during two cycles without interruption of a limestone (Fig. 4). The reason for the missing evaporitic limestone lies in the weak expression of climate precession and the interference of precession and obliquity in the northern summer insolation time series between 6.00 and 5.95 (Fig. 4).

The second limestone and underlying 4 cm alternation of limestones and calcareous marls represent the homogeneous bed of cycle M130 whose top is dated at 5.96 Ma (Fig. 4). The sedimentation rate decreases slightly above the second limestone, but otherwise remains constant as is suggested by the roughly equal thickness of the diatomite beds between the third to fifth limestone. The top of the limestones in cycles M131–132 are tuned to the insolation minima at 5.94 Ma and 5.92 Ma, and the base of the limestone in cycle M133 at 5.91 Ma (Fig. 4).

4.4. Planktonic foraminiferal zones and events

Figure 5 shows the semi-quantitative distribution of the keeled and unkeeled globorotaliids together with the neogloboquadrinids and their coiling direction. Added are samples whose planktonic foraminifers consist entirely of *Turborotalita quinqueloba* (see Appendix 5 for all microfossil data). The keeled globorotaliids provide two primary bioevents around the T/M boundary: the FO level of *G. miotumida* just above and the LO of *Globorotalia menardii* form 5 immediately below sapropel M73 where the first mentioned bioevent marks the base of biozone 11 as defined in Zachariasse et al. (2011). The unkeeled globorotaliids are subdivided into *Globorotalia ventriosa* (low to high-convex types with compact chambers and random coiling), *Globorotalia nicolae* (inflated chambers and dominant right coiling), and the extant *Globorotalia scitula* (small sized and dominant right coiling). Neogloboquadrinids show dominant left coiling up to the top of cycle M112 and right coiling above this level except in a short interval from top

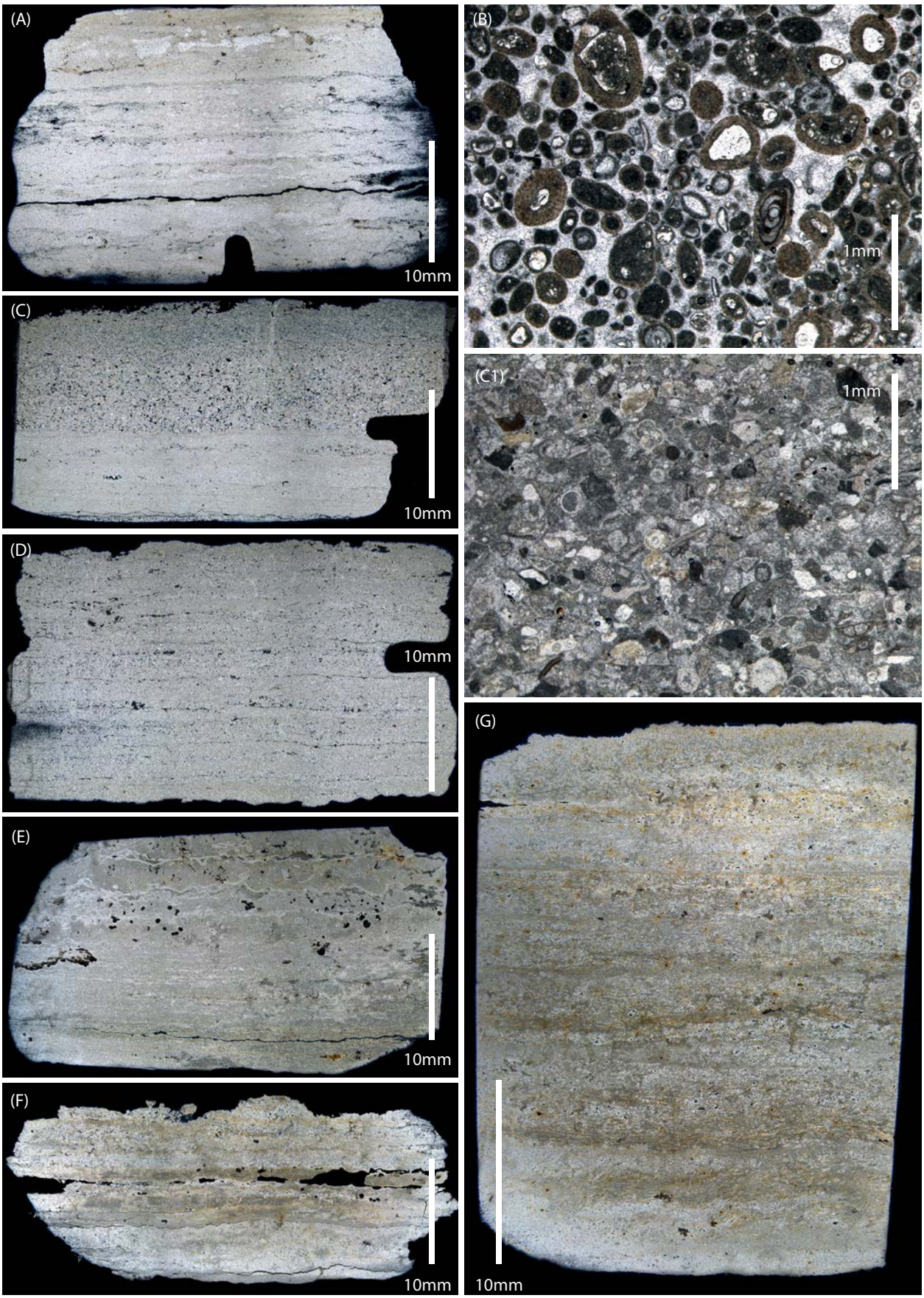

20220728-121929
A17159/66424/83D369E2

Plate 2. Thin section images of limestones in the top part of section Metochia: (A) Top first limestone (GR 12586b); (B) Second limestone (GR 12589); (C) Second limestone (GR 12590) with close-up of upper part in C1; (D) Third limestone (GR 12597). Idem in section Falconara: (E) First limestone (FA18–13); (F) Base third limestone (FA18–21); (G) Top third limestone (FA18–22).

M122 to base M123 where left coiled specimens dominate again. The LO and FO of *G. nicolae* and coiling shift in neogloboquadrinids are used here to define three new planktonic foraminiferal zones in addition to the eleven zones defined in Zachariasse et al. (2011) (for definition and ages of the 14 biozones, see Appendix 6). Zone 12 is the interval between FO and LO of *G. nicolae* and overlies the previously defined zone 11 between FO of *G. miotumida* (base) and FO of *G. nicolae* (top). Zone 13 is the interval between top zone 12 and the coiling shift in neogloboquadrinids (from left to right) and zone 14 extends from top zone 13 to the top of the marine Messinian. Bioevents 14a–e refer to five short-lived occurrences of neogloboquadrinids in the upper part of zone 14 with event 14a being characterized by dominant left coiling (cycles M122–123) and event 14c by 20–30 % left coiling (cycle M125). Both events equate with bioevents 8 and 9 in Krijgsman et al. (1999a). Bioevents 14b and 14d in cycles M124 and M129 are defined by the brief presence of 100 % right coiled neogloboquadrinids and by *G. scitula* in the case of bioevent 14b. Finally, bioevent 14e refers to the presence of 76 % right coiled neogloboquadrinids in a thin marl layer within the second limestone.

5. Discussion

5.1. The isotope curves and their interpretation

Oxygen and carbon isotope values for the pre-evaporitic Messinian are plotted in Fig. 6. The most remarkable change is the shift to heavier planktonic and benthic $\delta^{18}O$ values between cycles M91–M94 with poor coverage in between (Fig. 6). This change is dated at 6.74 ± 0.04 Ma and is greater for the benthic than planktonic values resulting in a larger difference between benthic and planktonic $\delta^{18}O$ from M94 upwards (Fig. 6). A second, more modest, change is the shift to lighter respectively heavier $\delta^{18}O$ values for planktonic and benthic foraminifers between cycles M108–M112 with poor coverage in between (see Fig. 6). This change is dated at 6.38 ± 0.03 Ma.

The change at 6.74 ± 0.04 Ma is visualized in average planktonic and benthic $\delta^{18}O$ values of 0.19‰ and 1.13‰ for cycles M73–M91 and values of 1.16‰ and 2.85‰ for cycles M94–M108, i. e. average planktonic and benthic values become 0.97‰ respectively 1.72‰ heavier at 6.74 ± 0.04 Ma (see dotted lines in Fig. 6). Average planktonic and benthic $\delta^{18}O$ values further change to –0.03‰ and 3.22‰ between cycles M108 and M112, i. e. average $\delta^{18}O$ values become 1.19‰ lighter respectively 0.37‰ heavier at 6.38 ± 0.03 Ma (Fig. 6).

Planktonic and benthic oxygen isotope values are relatively close to each other over the interval M73–M91 and further apart from M94 upwards (Fig. 6). The $\delta^{18}O$ difference of 0.94‰ between the average planktonic and benthic $\delta^{18}O$ values for the M73–M91 interval likely reflects a surface to deep water T difference of 4.3 ± 0.2 °C using the paleotemperature equations of Shackleton (1974) and Bemis et al. (1998). This T difference seems a reasonable estimate given the reconstructed depositional depth of around 1000 m for the Metochia site but is 1.5–2 °C smaller than for the modern eastern Mediterranean (Kassis and Korres 2020).

If the 0.97‰ respectively 1.72‰ shift to heavier average planktonic and benthic $\delta^{18}O$ values at 6.74 ± 0.04 Ma was to be explained by temperature then the surface water should have cooled by 4.5 ± 0.2 °C and the deep water by 7.9 ± 0.4 °C but literature-based evidence for cooling (which must have been particularly noticeable in the source area(s) of deep water formation considering the much stronger cooling of the deep water) is absent. The only well-dated regional T record available just shows the opposite: Mediterranean surface water cooled during the latest Tortonian and earliest Messinian but warmed at 6.7 Ma and remained warm until 6.3 Ma (Tzanova et al. 2015). Since ice volume changes are small around 6.74 ± 0.04 Ma (e. g. Drury et al. 2018), the shift to heavier planktonic and benthic foraminiferal $\delta^{18}O$ values should signal a rise in salinity caused by less outflow of deep salty Mediterranean water due to decreased sill depth (see also calculations and modelling results in Meijer 2006, Topper and Meijer 2015, Rohling et al. 2008). Less outflow and constant net evaporation should have resulted in less inflow of Atlantic surface water to conserve volume and salt. Superimposed on

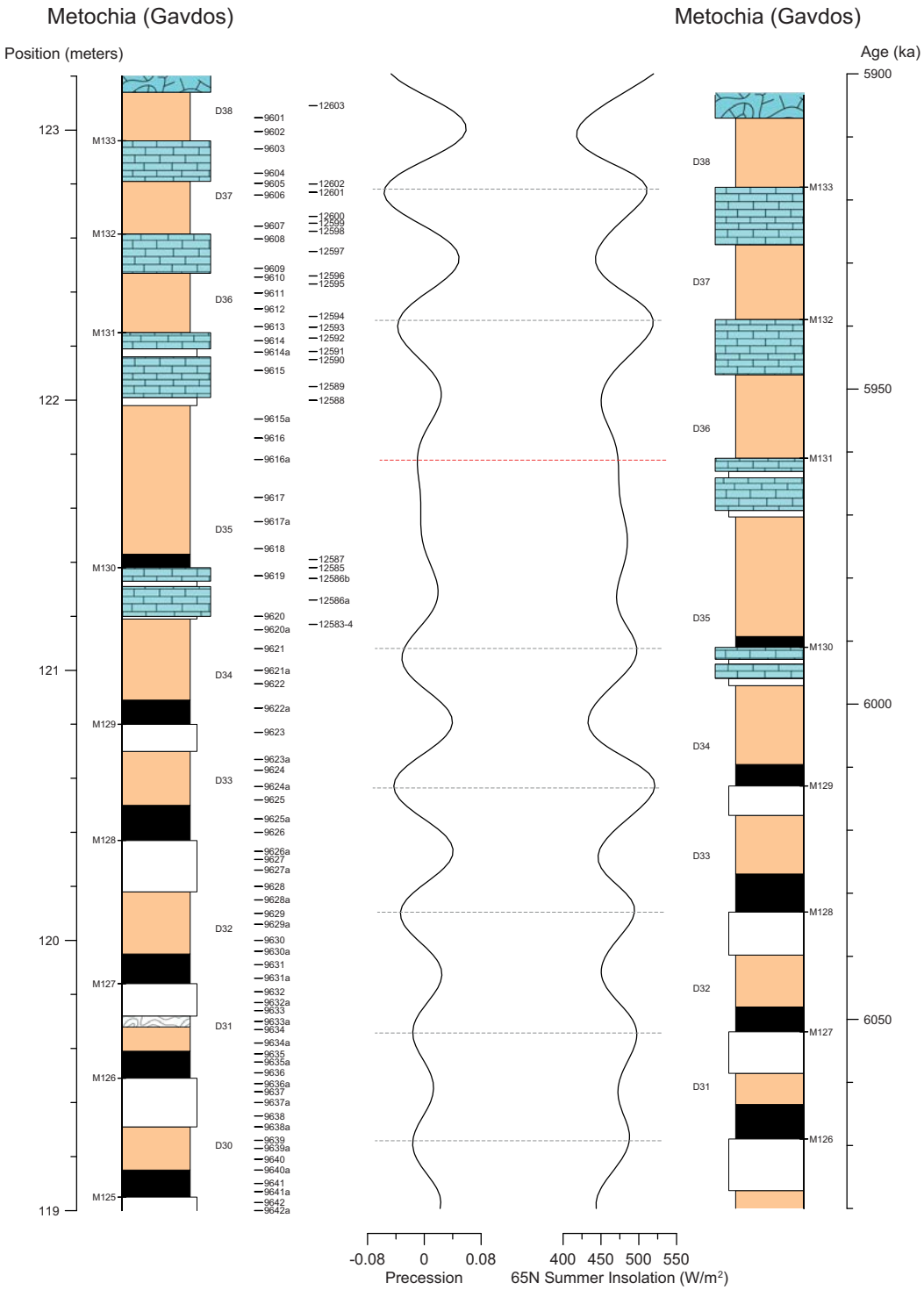

Fig. 4. Lithology and sample positions for the uppermost part of section Metochia based on Krijgsman et al. (1999a) and this study (samples GR 12583–GR 12603). The tuned section is shown at the right.

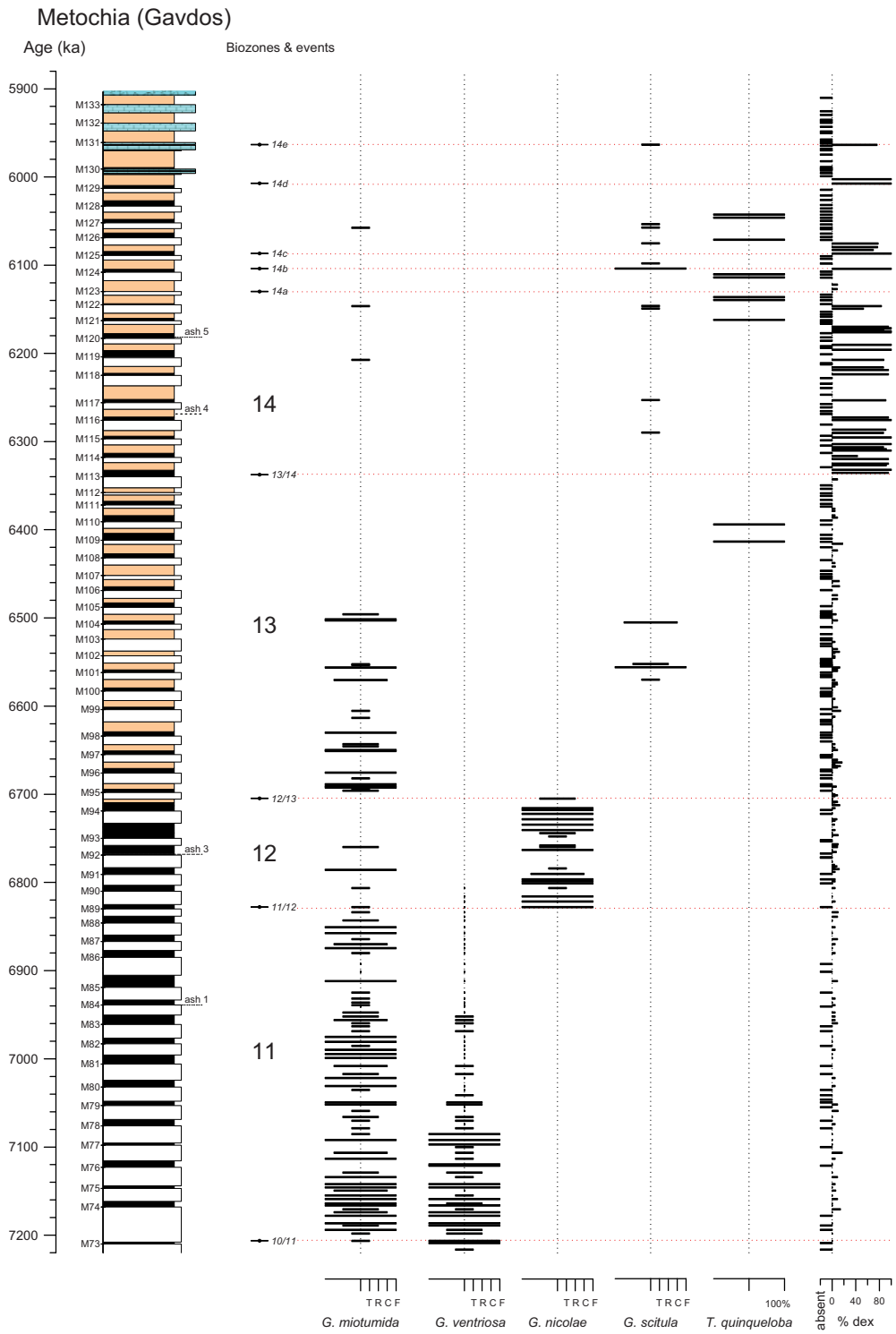

Fig. 5. Time-stratigraphic distribution of *G. miotumida*, *G. ventriosa*, *G. nicolae*, *G. scitula*, and *N. acostaensis* (and percent right coiling) in the Messinian of section Metochia based on semi-quantitative counts in 9 fields of a 45-field rectangular picking tray with F: > 20; C: 10–20; R: 3–10 and T: < 3 and >1 specimens in 27 fields. Separately indicated are monospecific planktonic foraminiferal faunas of *Turborotalita quinqueloba* (*T. multiloba* of authors). Planktonic foraminiferal zonal boundaries 10/11 to 13/14 and bioevents 14a–e in the upper part of zone 14 are defined in text.

20220728-121929
A17159/66424/83D369E2

the permanent decrease in outflow and inflow are ongoing precession-scale variations in the net volume flow of freshwater which cause negligibly small decreases (during maxima in northern summer insolation) and increases (during minima) in the inflow of Atlantic surface water as well as in the outflow and possibly the salinity of the outflow. As a result of the permanent decrease in outflow, not only will the salinity increase, but also the residence time of Mediterranean water and that is exactly what is recorded by the $\delta^{13}C$ values: they become depleted at 6.74 ± 0.04 Ma (Fig. 6). Why the depletion is greater in the planktonic than benthic $\delta^{13}C$ record is not yet fully understood.

Enrichments in the $\delta^{18}O$ and depletions in $\delta^{13}C$ of the benthic foraminifer *Planulina ariminensis* and planktonic foraminifer *G. bulloides* at the 6.7 Ma level in section Abad in SE Spain (Fig. 1A) were interpreted in the same way, viz. increasing salinity and residence time due to reduced outflow (Sierro et al. 2003). The coverage in the Abad section, however, is poor with only three data points between 6.9 and 6.7 Ma and not much isotope data above the 6.7 Ma level except the non-descript data set for *Orbulina* (see Fig. 7 in Sierro et al. 2003). Large enrichments in bulk benthic and planktonic foraminifers $\delta^{18}O$ across the M92–M93 equivalent time interval in section Monte del Casino in N Italy (for location, see Fig. 1A) were attributed to a combination of cooling and increased salinity whereas the simultaneous depletion in $\delta^{13}C$ follows a longer term trend explained in part by restricted outflow (Kouwenhoven et al. 1999). Superimposed depletions in $\delta^{18}O$ and enrichments in $\delta^{13}C$ above the 6.74 ± 0.04 Ma level may be related to a varying state of preservation of the foraminiferal samples in section Monte del Casino (see Fig. 7 in Kouwenhoven et al. 1999).

The 0.97‰ respectively 1.72‰ enrichment in average planktonic and benthic $\delta^{18}O$ values at the 6.74 ± 0.04 Ma level in section Metochia would correspond with a salinity increase of 3.9 ± 0.4 psu for the surface water and 6.9 ± 0.8 psu for the deep water (~1000 m) using the $\delta^{18}O_w$/salinity relationship for the modern Mediterranean of Pierre (1999) and Cox et al. (2011) and assuming that $\delta^{18}O_{calcite}$ is in equilibrium with $\delta^{18}O_w$ (see in chapter 3). Of course, these figures are approximations because standard deviations on the average oxygen isotope values are large (0.4–0.7‰) and the slope of 0.25 ± 0.03 for the modern Mediterranean $\delta^{18}O_w$/salinity relationship (op. cit.) is likely not the same in the early Messinian. The current slope is low compared to that of the adjacent Atlantic due to the excess evaporation in the Mediterranean (Pierre 1999). Excess evaporation in the early Messinian Mediterranean was probably smaller and the slope of the $\delta^{18}O_w$/salinity relationship somewhat steeper due to the more humid climatic conditions in the Late Miocene (Bertini and Menichetti 2015, Sachse 1997).

Assuming that the surface to deep water T difference of 4.3 ± 0.2 °C remained the same, then the increase in salinity at 6.74 ± 0.04 Ma is 3.0 ± 0.4 psu greater for the deep water than for the surface water (corresponding with the extra enrichment in the benthic $\delta^{18}O$ of 0.75‰ in Fig. 6). This increased difference between surface to deep water salinity after 6.74 ± 0.04 Ma suggests that surface water salinities in the area of deep water formation should have been periodically significantly higher than in adjacent areas of the EMED. The main drivers of intermediate and deep water formation in the modern EMED are salinity respectively temperature resulting in more or less similar surface and deep water salinities and slightly higher salinities at intermediate depth. If the formation of all the subsurface water in the Messinian was mainly salinity driven and formed in a small source area with strong evaporation (e. g. in the far northeast) then a somewhat larger salinity difference between surface and deep water is conceivable. The more humid conditions compared to today (Bertini and Menichetti 2015, Sachse 1997) indicate that the above scenario could only have played out during very dry spells in the deep water source area. Another possibility is that the restriction-imposed salinity increase occurred mainly in the deep water.

EMED salinities in the period from before the increase at 6.74 ± 0.04 Ma may have been reduced compared to modern values not only because of the more humid climatic conditions at that time (see above) but also because of a better exchange with the Atlantic during the Early Messinian (see paleogeographic reconstructions of the gateway area in Sissingh 2008 and Krijgsman et al. 2018). Assuming that EMED salinities before 6.74 ± 0.04 Ma were 1 psu reduced compared to the modern range of 38–39 psu for the EMED then a salinity increase of 3.9 ± 0.4 psu for the surface and 6.9 ± 0.8 psu for the deep water (using modern slope values, see above) would have brought salinities into the range of hypersaline values of >40 psu after 6.74 ± 0.04 Ma. Above we have argued that the slope of the $\delta^{18}O_w$/salinity relationship for the Early Messinian Mediterranean was probably somewhat steeper but even at a 20 % steeper slope, salinities would still reach hypersaline values.

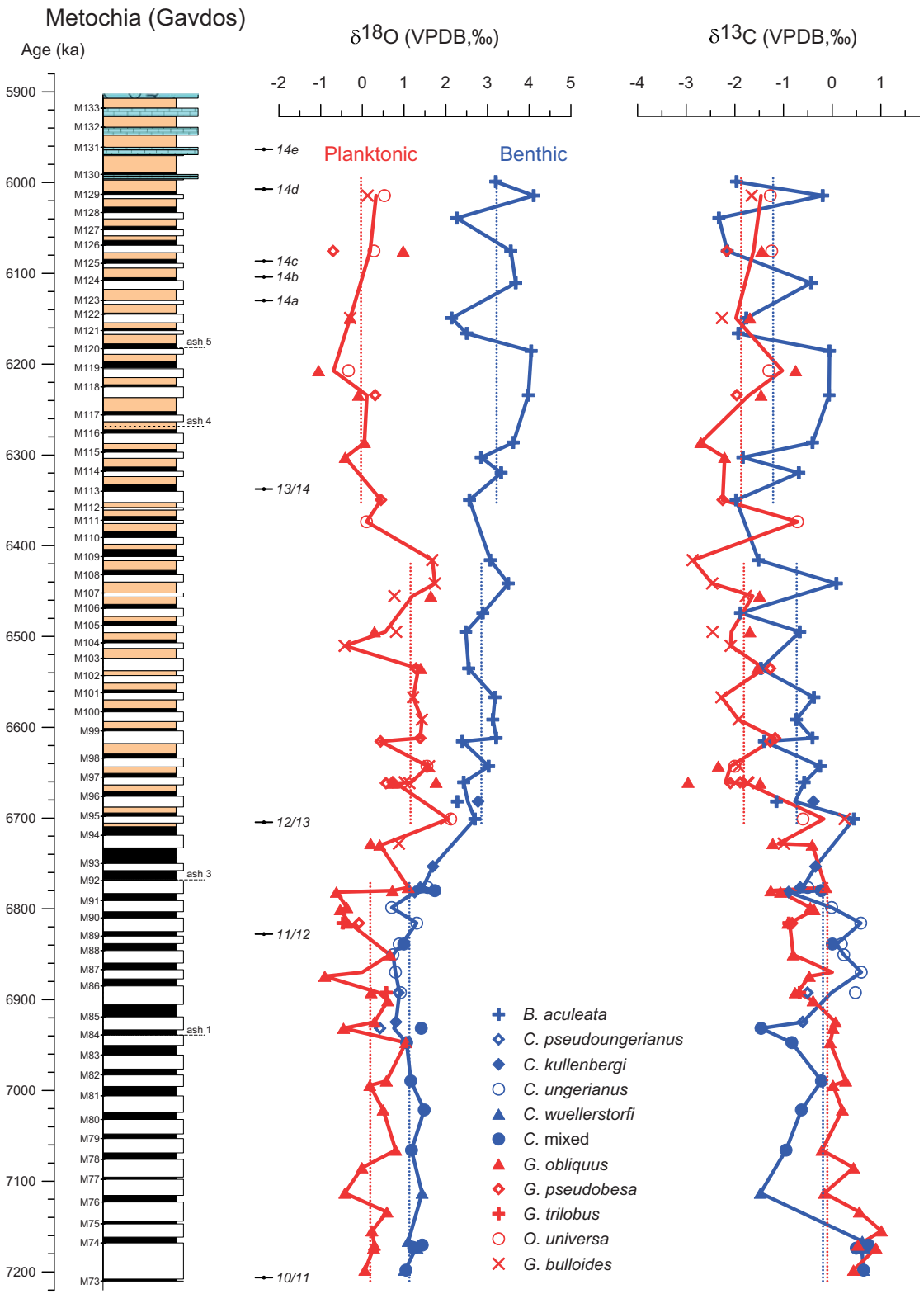

Fig. 6. Oxygen and carbon isotope curves for the pre-evaporitic Messinian in section Metochia based on data collected in this study and that of Seidenkrantz et al. (2000). All data are from homogeneous marl beds. Isotope values are normalized to *C. wuellerstorfi* and *G. obliquus* and plotted versus time. Dotted lines represent average values for three different intervals corresponding with cycles M73–M91, M94–108 and M112–129.

20220728-121929
A17159/66424/83D369E2

The heaviest values for the benthic $\delta^{18}O$ in section Metochia occur in the interval above the 6.38 ± 0.03 Ma level whereas planktonic $\delta^{18}O$ measurements return to values from before 6.74 ± 0.04 Ma (Fig. 6). The enrichment in average benthic $\delta^{18}O$ across the 6.38 ± 0.03 Ma level of 0.37‰ suggests a further rise in deep water salinity of 1.5 ± 0.2 psu using modern $\delta^{18}O_w$/salinity slope values. The return of planktonic oxygen isotope values to pre-6.74 ± 0.04 Ma values is not well understood but could reflect diminished rates of mixing between low-saline surface and hypersaline subsurface water during wet spells in periods of prevalent dry conditions and homogeneous marl deposition.

Obviously, more isotope data, especially from shallower marine basins, are needed to better constrain the magnitude of the increase in salinity at 6.74 ± 0.04 Ma. A saltier Mediterranean of course remains subject to precession-scale variations in the freshwater budget with reduced surface water salinities and suppression or weakening of deep water formation at times of maximum northern summer insolation.

Fig. 7. The Falconara section with sedimentary cycles (T for Tripoli Fm) and samples after Hilgen and Krijgsman (1999). The tuned section is modified from Hilgen and Krijgsman (1999) and Krijgsman et al. (1999a) by using the La2004 solution and shown at the right together with the distribution of *G. miotumida*, *G. ventriosa*, *G. nicolae*, *G. scitula*, *T. multiloba* and *N. acostaensis* (and percent right coiling) based on semi-quantitative counts by Hilgen and Krijgsman (1999). Note that the labelling of the unkeeled globorotaliids (*G. scitula* group and *G. nicolae* in Hilgen and Krijgsman 1999) is alligned with that in section Metochia. Bioevents in Hilgen and Krijgsman (1999) are marked by capital letters at far right side. Corresponding planktonic foraminiferal zones and bioevents defined in section Metochia are shown immediately to the right of the column. The Hilgen and Krijgsman (1999) samples (with prefix JT) are replenished by new (FA) samples collected by Frits Hilgen in 2018. In this study, we analyzed the microfossils in all JT and FA samples from cycle T41 upwards and added the semi quantitative data on the distribution of neogloboquadrinids and *G. scitula* to Figure 7 (for the full data set, see Appendix 8). The Hilgen and Krijgsman (1999) and new data show that bioevent 14d falls in the cycle with the first limestone in the FA sample set in accordance with the position of the first limestone in Blanc-Valleron et al. (2002). Asterisk marks the first limestone in Hilgen and Krijgsman (1999).

5.2. Biotic response to the salinity increase at 6.74 ± 0.04 Ma and 6.00 Ma

The salinity increase, to values in the hypersaline range, has left a clear mark on the benthic foraminiferal faunas from the homogeneous marl beds. They are diverse before and low-diverse and less numerous after the salinity increase at 6.74 ± 0.04 Ma. Epifaunal species as *C. kullenbergi*, *C. pseudoungarianus*, *P. ariminensis*, *Gyroidina soldanii*, and several *Uvigerina* species vanish around the 6.72 Ma level (see also Seidenkrantz et al. 2000) whereas the salt-tolerant *B. aculeata* (Kouwenhoven et al. 2006) often becomes dominant or even is the only in-situ species present in the homogeneous marl beds above the 6.72 Ma level. Benthic faunas from the laminated marls, on the other hand, show no obvious change: they are made up of low-oxygen tolerant species and allochthonous shallow water species though relative numbers of the latter group increase after the 6.74 ± 0.04 Ma level.

The planktonic foraminiferal faunas that date from after the salinity increase are less diversified and often dominated by one or two species (Appendix 5). Unkeeled globorotaliids are sparsely present above the 6.72 Ma level and represented by few intermittent occurrences of *G. scitula* whereas *G. miotumida* remains intermittently common up to cycle M104 (Fig. 5). Remarkable similar patterns are reported from the Messinian in sections Falconara in Sicily (Fig. 7) and Abad in SE Spain (Fig. 8).

In section Ain el Beida on the Atlantic margin of Morocco (corresponding with Metochia cycles M108–M133), *G. scitula* is continuously present whereas *G. miotumida* is common up to the level equivalent to Metochia cycle M116 (for location of Ain el Beida, see Fig. 1A; for the Ain el Beida planktonic foraminiferal data and calibration to Metochia, see Krijgsman et al. 2004). Both species are deep dwellers (Hemleben et al. 1989) and their early vanishing from the Mediterranean suggests that salinities reached values at or beyond the maximum for these species to sustain viable populations. The same could apply for the absence of *Globoturborotalita nepenthes* above cycle M99 and the long periods of absence over cycles M94–M113 and the virtual absence above cycle M113 of *G. trilobus* in section Metochia (Fig. 5 and Appendix 5). The latter species shows a comparable pattern in the Abad section (Sierro et al. 2003) but both these species are not listed from the Ain el Beida section.

The increase in salinity at 6.74 ± 0.04 Ma affected the neogloboquadrinids as well because samples with neogloboquadrinids become twice as rare above the

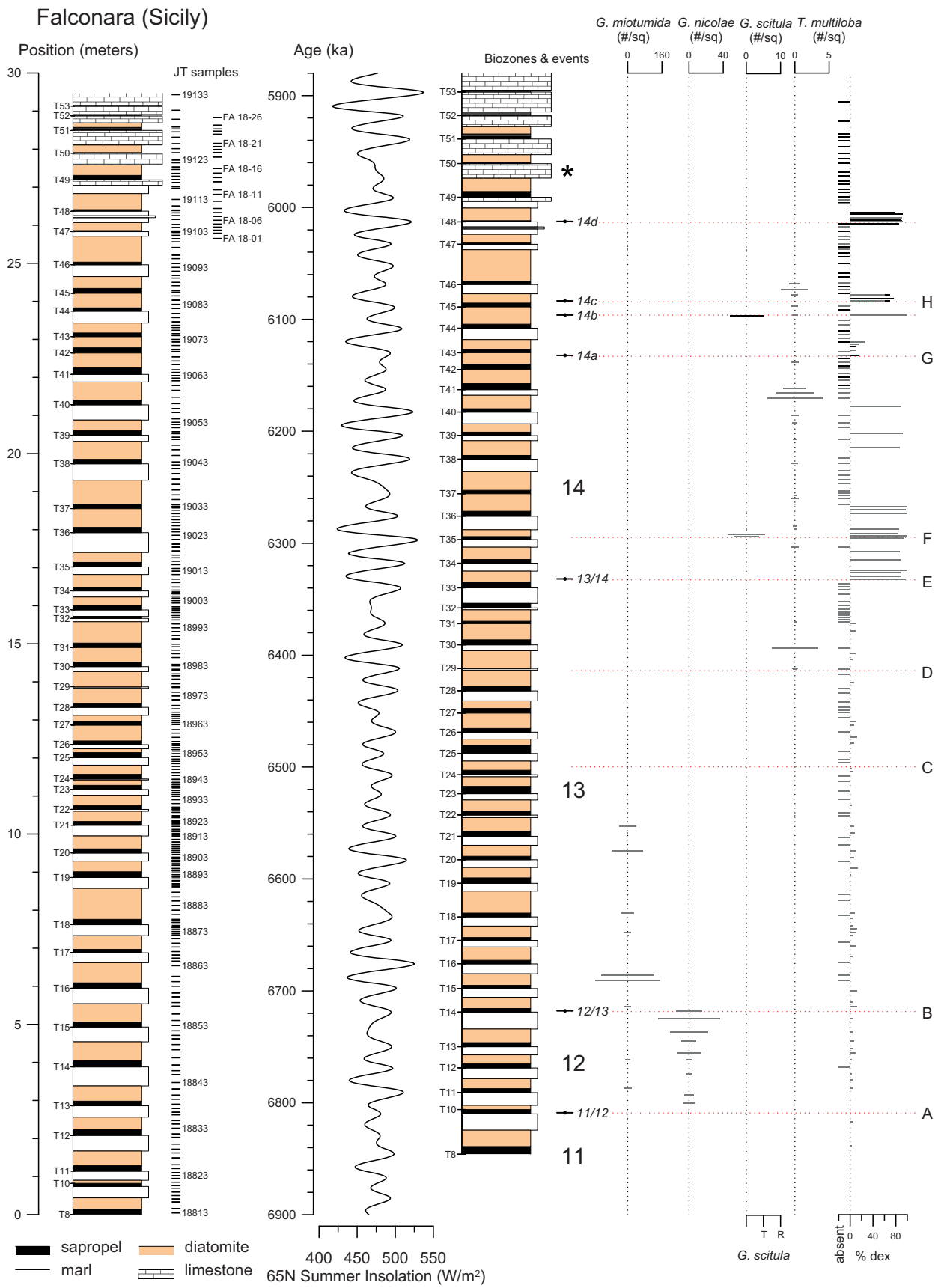

20220728-121929
A17159/66424/83D369E2

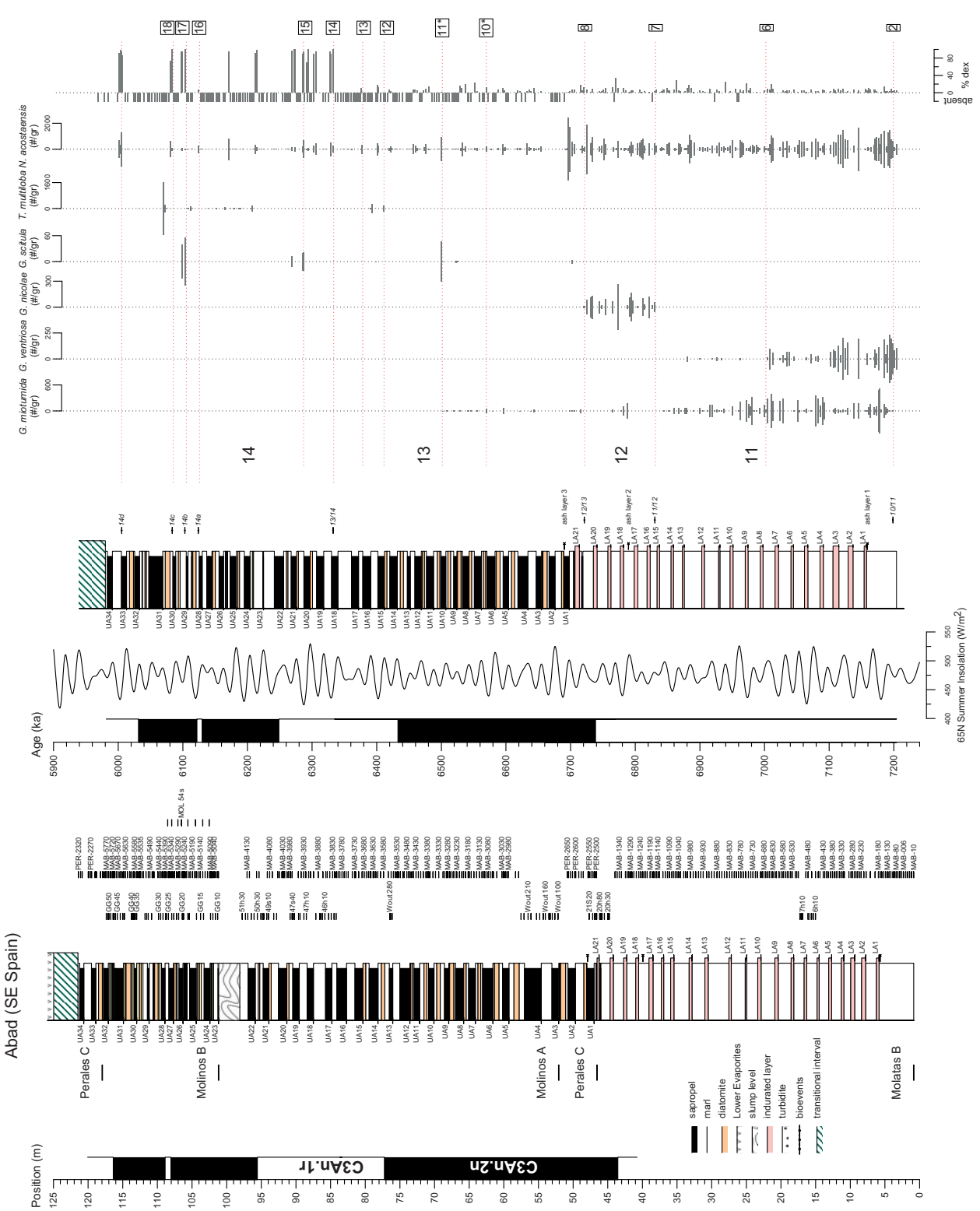

20220728-121929
A17159/66424/83D369E2

Fig. 8. The Abad composite section with sedimentary cycles (LA for Lower Abad and UA for Upper Abad marls) and identified polarity intervals after Krijgsman et al. (1999a) and Sierro et al. (2001). The tuned section is modified from Krijgsman et al. (1999a) and Sierro et al. (2001) by using the La2004 solution and shown at the right together with the distribution of *G. miotumida*, *G. ventriosa*, *G. nicolae*, *G. scitula*, *T. multiloba* and *N. acostaensis* (and percent right coiling) based on the data in Sierro et al. (2001). Note that the labelling of the unkeeled globorotaliids (*G. scitula* group in Sierro et al. 2001) is alligned with that in section Metochia. Numbered bioevents in Sierro et al. (2001) are shown at the far right side. Corresponding planktonic foraminiferal zonal boundaries 10/11 to 13/14 and bioevents 14a–c defined in section Metochia are shown immediately to the right of the tuned section. The highest (unnumbered) spike of dextral neogloboquadrinids in Sierro et al. (2001) corresponds with bioevent 14d.

M92–M93 interval than below it (Fig. 5 and Appendix 5). A similar pattern is shown in section Abad (Fig. 8). Frequency data for neogloboquadrinids in section Falconara only cover a short interval below the 6.74 ± 0.04 Ma level but the pattern above shows many absence intervals as well (Fig. 7). All this suggests that the salinity increase at 6.74 ± 0.04 Ma caused the neogloboquadrinids to be more often absent in the Mediterranean. In section Ain el Beida, however, neogloboquadrinids are continuously present with dominant left coiling in the basal 5 cycles and right coiling in the next 39 cycles albeit with several short-lived interruptions of left coiled assemblages (Krijgsman et al. 2004). This left to right coiling shift in section Ain el Beida is time-equivalent with the left to right coiling shift and 13/14 zonal boundary in sections Metochia, Falconara and Abad because it occurs in the fourth cycle below base Chron C3An.1n in sections Ain el Beida (Krijgsman et al. 2004) and Abad (Fig. 8) and in the nineteenth cycle above the 12/13 biozonal boundary in sections Metochia and Abad (Fig. 5 and 8). Also the short re-occurrence of dominant left coiled neogloboquadrinids in Metochia cycle M123 (bioevent 14a) and time-equivalent cycles in sections Falconara (Fig. 7) and Abad (Fig. 8) shows up in section Ain el Beida (Krijgsman et al. 2004) indicating that the coiling changes associated with bioevent 14a and the base of biozone 14 are generated by shifts in the areal distribution patterns of right and left coiled populations in the adjacent Atlantic.

The recurrent absence of neogloboquadrinids in cycles M108–M113 of section Metochia and their continuous presence over the same interval in section Ain el Beida (cycles AeB 1–25, see Krijgsman et al. 2004) implies that variable conditions within and not outside the Mediterranean governed the absence/presence pattern of neogloboquadrinids in section Metochia. These variable conditions should have controlled the presence or absence of a Deep Chlorophyll Maximum (DCM) because it has been shown by Fairbanks et al. (1980) and Ravelo et al. (1990) that the preferred habitat of modern neogloboquadrinids is in the DCM.

A DCM layer will develop during precession-scale wet periods and laminated sediment deposition but breaks down in the prevalent dry periods of homogeneous marl deposition (for relationship between neogloboquadrinids in Quaternary laminated sediments and DCM, see for example Rohling and Gieskes 1989, Lourens et al. 1992). The absence/presence pattern of neogloboquadrinids in the interval of cycles M108–M113, however, does not simply follow a homogeneous to laminated marl pacing. Absence intervals may start in homogeneous and end in laminated, or vice versa, or they are restricted to laminated, or extend across one or more couplets (Appendix 5). All these departures from the simple homogeneous versus laminated pattern indicate that presence or absence of neogloboquadrinids is controlled by a complex interplay between restocking from the Atlantic and DCM development in the Mediterranean with no DCM in very dry periods and perhaps an expanded but less productive DCM layer in wet periods during which the increased surface-deep water salinity gradient diminished or even blocked deep water formation thereby reducing the slow upward flow of nutrients.

Yet another difference between the planktonic fauna from before and after the salinity increase at 6.74 ± 0.04 Ma is the intermittent presence of monospecific planktonic foraminiferal faunas of *Turborotalita quinqueloba* from cycle M108 upwards (Fig. 5). Time-equivalent counterparts are reported from sections Falconara (Fig. 7 and Blanc-Valleron et al. 2002) and Abad (Fig. 8). They occur both in homogeneous and laminated beds and likely point to extremely high and low salinities because no such monospecific assemblages are reported from section Ain el Beida.

Samples with no or few planktonic foraminifers in Metochia (Appendix 5) and Abad section (Sierro et al. 2003) likely represent short periods with extremely high or low salinities as well. Studies on Red Sea cores have shown that salinities above 45 psu are adverse for planktonic foraminifers and lethal beyond 49 psu (Rohling et al. 1998, Fenton et al. 2000). Such salinity

values are consistent with the inferred hypersaline conditions after 6.74 ± 0.04 Ma with salinities possibly exceeding 45 psu during extremely dry spells in periods of minimum northern summer insolation. Levels with no or few planktonic foraminifers in laminated beds probably point to extremely low-saline surface water (perhaps close to planktonic foraminifer-free Black Sea surface water values of 18 psu) due to poor winter mixing of the low-salinity summer surface layer with the hypersaline water below.

The salinity increase at 6.74 ± 0.04 Ma is also accompanied by the introduction of diatomites from cycle M94 upwards (Fig. 2). The many diatoms shown in a few smear slides justify the term diatomite for these laminated marls. Radiolarians are characteristic microfossils in the washed residues from diatomites just as the spicules of siliceous sponges but the latter are not limited to the diatomites alone and enter the record a little earlier than diatomites and radiolarians (Appendix 5). The sudden introduction of diatomites and siliceous microfossils at 6.72 Ma should be attributed to a change in the processes governing surface water productivity every ~21 kyr after 6.72 Ma (e. g. as in the model of Filippelli et al. 2003) and this change should be related in some way to the abrupt decrease in outflow and concomitant increase in salinity and residence time of the Mediterranean. The introduction of the spicules of bottom dwelling siliceous sponges at about the same time suggests a role for silica preservation as well.

A further rise in salinity is marked by the onset of evaporitic limestone formation at 6.00 Ma (Fig. 2 and 4). This time, salinity should have exceeded 70 psu since calcium carbonate precipitates at 72 psu (Usiglio 1849). The diatoms, radiolarians and siliceous sponge spicules in the diatomites between the evaporitic limestones (see Appendix 5) indicate that surface water salinities were sufficiently reduced at times of minimum precession to enable the re-invasion of these marine biota from the Atlantic. The few and dwarfed benthic foraminifers that remain present are mainly bolivinids and ex situ shallow water species. The highest occurrence of *B. aculeata* is in the 5 cm thick marl layer of the second limestone (GR 12591 in Fig. 4 and Appendix 5). Planktonic foraminifers are essentially absent in between the limestones except the poorly preserved and dwarfed association in the marl layer within the second limestone with among others rare (76% dextral) neogloboquadrinids and traces of *G. scitula* (Appendix 5). In the absence of clearly reworked elements, these neogloboquadrinids are considered in situ and thus represent the youngest known occurrence in the Messinian Mediterranean (termed bioevent 14e in Fig. 5). Noteworthy are rare pteropods (mostly molds) up into the diatomite above the third limestone of cycle M132 (Appendix 5). Pteropods from the clayey layer on top of the first limestone (GR 12585 in Fig. 4) may belong to the genus *Vaginella* and those from the diatomite above the second limestone of cycle M131 (GR 12595 in Fig. 4) to *Creseis* aff. *spina* (determinations by A. W. Janssen, November 2003).

Remarkable are the (molds of) planktonic larval shells of benthic Mollusca (with bivalves dominating over gastropods) in between the limestone beds (determination by A. W. Janssen, November 2003). These juveniles must have been transported seawards from their neritic parent populations but their settling in deep water prevented them to complete their life cycle. Why their occurrence is restricted to the limestone interval is unclear.

5.3. An evaluation of the currently used ages for onset MSC in three other key sections

The first salinity step at 6.74 ± 0.04 Ma from normal marine to hypersaline (>40 psu) is attributed by us to a decrease in Mediterranean outflow (chapter 5.1) and it is obvious to explain the second step from hypersaline to salinities above 70 psu and onset of evaporitic limestone formation on Gavdos by a further reduction in Mediterranean outflow as long as conditions of net evaporation are maintained. A further reduction in outflow and onset of gypsum formation at 140 psu (see Usiglio 1849, McCaffrey et al. 1987) would then be a logical next step.

Gavdos does not expose Messinian gypsum but laminated gypsum with intervening deep marine laminated marls are known from nearby Crete (Plate 1F–G) though the age for onset of gypsum formation on Crete is unknown, nor is it known if the gypsum is preceded by evaporitic limestones (desiccation and subaerial erosion removed parts or even all of the Lower Evaporites and what remained is often incorporated in Lower Pliocene debris flows; Zachariasse et al. 2008).

In the Sorbas Basin of SE Spain (section Perales, Fig. 1A) and in N Italy (section Monticino, Fig. 1A), the onset of the MSC is marked by gypsum formation. This first gypsum is dated at 5.971 Ma (Manzi et al. 2013) implying that calcium carbonates on Gavdos and

gypsum in SE Spain and N Italy precipitated simultaneously and not consecutively. Below we will evaluate the age for the first gypsum in the Perales and Monticino sections, as well as the age and origin of the first limestone in section Falconara (Sicily).

5.3.1. On the age of the first gypsum in section Perales

The Perales section represents the uppermost part of the Abad composite section of Krijgsman et al. (1999a) and Sierro et al. (2001) and is shown in Fig. 9 along with that of Manzi et al. (2013) and Mancini et al. (2020). The N/R reversal representing top Chron C3.An.1n falls in the sapropel of cycle UA32 and bioevent 14d in the top of sapropel UA33 (for the complete Abad composite section, see Fig. 8). Figure 9 shows that cycle UA33 equates with Metochia cycle M129 but in contrast with Gavdos no evaporitic limestone is present in the Perales section of Krijgsman et al. (1999a) and Sierro et al. (2001) though Manzi et al. (2013) figures an indurated layer in the upper part of UA33. Equating the top of this indurated layer of cycle UA33 with top of the first limestone in Metochia (dated at 5.99 Ma, see Fig. 4) implies that the lower part of cycle UA34 in the Perales section of Manzi et al. (2013) correlates with the laminated marls in Metochia cycle M130. Latter laminated marls are extra thick so we correlated the base of cycle M131 to the precession minimum at 5.96 Ma (see also Fig. 9 and discussion in 4.3). The lower part of UA34 in Manzi et al. (2013) includes two cycles as well: one extends from base UA34 to top indurated marl layer and the other from top indurated marl layer to top first gypsum (Fig. 9). In this interpretation of cycle UA34, the top of the first gypsum equates with top of second limestone on Gavdos providing an age of 5.96 for top and 5.97 Ma for base first gypsum. This age is similar to the currently used age of 5.971 Ma (Manzi et al. 2013).

The first gypsum in the Perales section of Manzi et al. (2013) is figured lateral to limestone and the same is suggested in Mancini et al. (2020) but latter authors show two thinly bedded limestones below the first gypsum-limestone bed (Fig. 9). The study of Roveri et al. (2020) shows that the limestone associated with the first gypsum as well as the limestones below and above are not evaporitic but calciclastic turbidites with the detritus supplied from a carbonate platform at the Sorbas Basin margin. These turbidites interfinger with the evaporitic gypsum beds basin inwards.

5.3.2. On the age of the first gypsum in section Monticino

Our analysis of the Krijgsman et al. (1999b) samples from section Monticino yielded (in addition to some reworked planktonic and epifaunal benthic foraminiferal species up to the second respectively third limestone) irregular occurrences of neogloboquadrinids that (we believe) are in situ and the key in correlating section Monticino to Metochia on Gavdos (Fig. 9 and Appendix 7). The 85 % dextral neogloboquadrinids in the first cycle above the R/N reversal at top Chron C3An.1n may equate with bioevent 14d and the neogloboquadrinid occurrences below the N/R reversal with bioevents 14a–c but requires that the equivalent of Perales cycle UA31 is missing in section Monticino (Fig. 9). The hiatus is likely tectonic in nature just as the tectonic reductions reported by Krijgsman et al. (1999b) from below the limestones. Two remarks are pertinent here: 1) the coiling pattern of bioevents 14a–d is not fully consistent with that in section Metochia (compare Appendix 5 and 7) and 2) the limestones (marly limestones in the field notes of Krijgsman) are not evaporitic because they are washable and have foraminifers, fish debris and echinoid spines (Appendix 7). In our biocyclostratigraphic interpretation of section Monticino, the top of the fifth marly limestone equates with the top of Perales cycle UA33 and top Metochia cycle M129 (Fig. 9). The sixth marly limestone may then correlate with the indurated marl layer within cycle UA34 of Manzi et al. (2013) (Fig. 9). If true and if no strata are missing in the disturbed uppermost part (see deformation on photograph in Figure 4 of Manzi et al. 2013) then the top of the first gypsum bed equates with the top of the second limestone on Gavdos providing an age of 5.96 Ma for top and 5.97 Ma for the base of the first gypsum in section Monticino.

5.3.3. On the age and origin of the first evaporitic limestone in section Falconara

Figure 9 shows that bioevent 14d falls in the cycle with the first limestone (for the complete Falconara section, see Fig. 7). The six limestones in section Falconara are finely bedded to massive without clear evidence for normal grading or cross bedding. Thin sections from the old (with prefix JT, see Fig. 7) and new (FA) samples (Fig. 7) show lime mud with mm-scale layering without coarser layers or bioclasts. Spar occurs in the form of small bright speckles. Layering is irregular

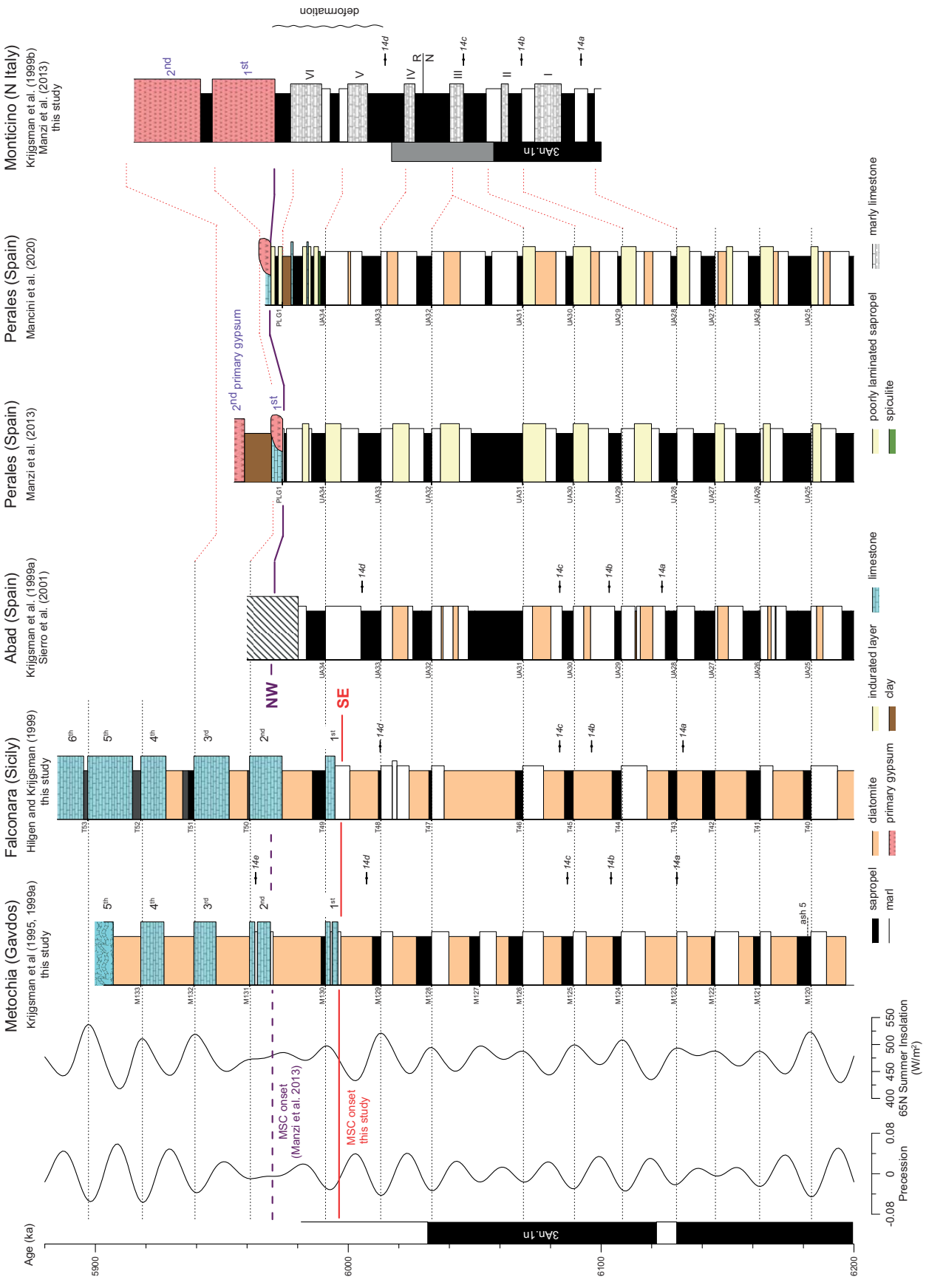

20220728-121929
A17159/66424/83D369E2

Fig. 9. Lithology and UA cycles of the uppermost Abad composite section and the Perales subsection after different authors. Correlation to the uppermost part of sections Metochia and Falconara is straightforward up to base UA34 using the positions of bioevents 14a–d. For the biocyclostratigraphy and tuning of the complete Falconara and Abad sections, see Fig. 7 and 8. For the complete biocyclostratigraphy and tuning of section Metochia, see Fig. 2 and 5. The first gypsum in the Perales section of Manzi et al. (2013) is equated with the second limestone in section Metochia. Lithology and magnetostratigraphy of section Monticino (N Italy) is based on Krijgsman et al. (1999b). Note that N/R in section Monticino refers to the redefined position of top C3An.1n by Manzi et al. 2013). Correlation between sections Monticino and Abad is based on the position of top C3An.1n and bioevents 14a–d in both sections. Note that limestones in section Monticino are marly and not evaporitic. SE: onset MSC in the central-eastern Mediterranean. NW: onset MSC in the northwestern part.

with darker layers being clayey (Plate 2E–F). We interpret these limestones as being evaporitic just as did Krijgsman et al. (1999a) and Blanc-Valleron et al. (2002). Appendix 8 shows that the marine microfaunas between the evaporitic limestones are poor in foraminifers but relative rich in siliceous microfossils, just as in section Metochia (Appendix 5). The tuning of section Falconara provides an age of 6.00 Ma for the base of the first of these evaporitic limestones (Fig. 9). This age is similar to that of the first one in section Metochia.

5.3.4. Differences in age for the onset of the MSC

Our stratigraphic analysis of the onset of the MSC in the sections discussed above indicates that the ages for the onset of the MSC and associated evaporite facies are different in the studied locations. The onset of evaporite formation in sections Metochia and Falconara begins at ~6.00 Ma with calcium carbonate precipitation whereas in sections Perales and Monticino, onset begins at 5.97 Ma with gypsum precipitation. Also in S Italy (e. g. Guido et al. 2007) and perhaps on Cyprus (referred to as stromatolitic limestones in Krijgsman et al. 2002), the MSC seems to begin with evaporitic limestones but onset is not well dated. Gypsum formation on the other hand marks the onset of the MSC not only in the Perales and Monticino sections but also in the Piedmont Basin of N Italy (Dela Pierre et al. 2016, Lozar et al. 2018) though our analysis of their published foraminiferal data does not allow a precise date for the onset probably due to reworking.

The tuning of the five evaporitic limestones on Gavdos suggests that gypsum precipitation started no earlier than ~5.90 Ma there, i. e. at least 100 kyr after the MSC onset on Gavdos and 70 kyr after the onset of gypsum formation in sections Perales and Monticino (Fig. 9). Even the onset of carbonate precipitation is diachronous and two or three cycles younger in section Capodarso (for location, see Fig. 1A), some 50 km away from Falconara (Hilgen and Krijgsman 1999). Evidently, onset and progression of the MSC is not governed solely by changes in gateway geometry and outflow because in that case evaporite formation would have occurred synchronously over the Mediterranean and carbonate and gypsum would have precipitated sequentially. Differences in ages for the onset of the MSC (with older ages in the central-eastern Mediterranean) and in the initial evaporite facies (calcium carbonates in the central-eastern Mediterranean and gypsum in the northwestern part) could be explained by the presence of sills as in the models of Selli (1973), Lugli et al. (2010) and Roveri et al. (2014a), Roveri et al. (2014b), Roveri et al. (2020) but recently published evidence for gypsum precipitation at salinities as low as 40 psu by inflow of calcium and sulfate-rich low-saline water from the Parathethys (Grothe et al. 2020) and regional surface water freshening in the northern Mediterranean (Sabino et al. 2020) provide additions to existing models. Clearly, more precise ages are needed for the first evaporites at other locations (e. g. Cyprus and Piedmont Basin) along with more biomarker and modelling studies to better understand the origin of the observed diachroneity in the onset of the MSC and the associated differences in evaporite facies.

6. Conclusions

Oxygen and carbon isotope values in planktonic and benthic foraminifers from the deep marine Messinian on Gavdos show abrupt changes at 6.74 ± 0.04 Ma which are interpreted to reflect an increase in salinity from normal marine to hypersaline due to reduced outflow of Mediterranean water.

The limestones on Gavdos are evaporitic and the onset of their formation at 6.00 Ma suggests an abrupt further rise in salinity to values above 70 psu.

The biotic response to this two-step increase of Mediterranean salinities is seen mainly in an impover-

ishment of planktonic and benthic foraminiferal faunas and their vanishing after the onset of evaporite formation but marine diatoms, radiolarians, siliceous sponge spicules and rare epiphytic benthic foraminifers remain present in between the evaporitic limestones and even between the gypsum on Crete indicating that Mediterranean surface water salinities in between the evaporites were sufficiently reduced to allow these marine organisms to re-invade from the Atlantic at times of maximum northern summer insolation.

The stratigraphic analysis of the onset of evaporite formation on Gavdos and three other key locations revealed that 1) our age of 5.97 Ma for the onset of gypsum precipitation (and of the MSC) in SE Spain (Perales) and N Italy (Monticino) is similar to the currently used age of 5.971 Ma, 2) the onset of the MSC on Gavdos and Sicily (Falconara) begins earlier, at 6.00 Ma, and not with gypsum but calcium carbonate precipitation, and 3) tuning of the five evaporitic limestones on Gavdos shows that gypsum formation on Gavdos started no earlier than 5.90 Ma, i. e. 70 kyr later than in the SE Spain (Perales) and N Italy (Monticino).

Acknowledgements. Arnold van Dijk is thanked for measuring the stable isotope samples. Frits Hilgen is thanked for making new lithological data and samples from Falconara available and Gioa Bezemer for washing and analyzing the new samples. Previews by Frits Hilgen, Wout Krijgsman and Paco Sierro are greatly appreciated and significantly improved the manuscript. Frank Huiskamp is acknowledged for his help and company on Gavdos in 2003. We further thank Paco Sierro and Wout Krijgsman for making the planktonic foraminiferal respectively paleomagnetic data of the Abad composite section available. Wout Krijgsman further provided lithological data and sample positions for the Monticino section. Arie W. Janssen made the determinations of the Pteropods and small benthic Mollusca from the laminated marls in between the limestones in Metochia. The thoughtful review by an anonymous reviewer was of great help in improving our manuscript. This research was carried out under the program of the Netherlands Earth System Science Centre (NESSC), financially supported by the Dutch Ministry of Education, Culture and Science (OCW).

References

Bemis, B. E., Spero, H. J., Bijma, J., Lea, D. W., 1998. Reevaluation of the oxygen isotopic composition of planktonic foraminifera: Experimental results and revised paleotemperature equations. Paleoceanography 13, 150–160.

Bertini, A., Menichetti, E., 2015. Palaeoclimate and palaeoenvironments in central Mediterranean during the last 1.6 Ma before the onset of the Messinian Salinity Crisis: A case study from the Northern Apennine foredeep basin. Review of Palaeobotany and Palynology 218, 106–116.

Blanc-Valleron, M.-M., Pierre, C., Caulet, J., Caruso, A., Rouchy, J.-M., Cespuglio, G., Sprovieri, R., Pestrea, S., Di Stefano, E., 2002. Sedimentary, stable isotope and micropaleontological records of paleoceanographic change in the Messinian Tripoli Formation (Sicily, Italy). Palaeogeography, Palaeoclimatology, Palaeoecology 185, 255–286.

Cox, K., Rohling, E., Schmidt, G., Schiebel, R., Bacon, S., Winter, D., Bolshaw, M., Spero, H., 2011. New constraints on the Eastern Mediterranean $\delta^{18}O$: δD relationship. Ocean Science Discussions 8, 39–53.

Dela Pierre, F., Natalicchio, M., Lozar, F., Bonetto, S. M. R., Carnevale, G., Cavagna, S., Colombero, S., Sabino, M., Violanti, D., 2016. The Northermost record of the Messinian salinity crisis (Piedmont Basin, NW Italy). Geological Field Trips 8 (2.1), 58 pp.

Drury, A. J., Westerhold, T., Hodell, D., Röhl, U., 2018. Reinforcing the North Atlantic backbone: revision and extension of the composite splice at ODP Site 982. Climate of the Past 14, 321–338.

Fairbanks, R. G., Wiebe, P. H., Bé, A. W., 1980. Vertical distribution and isotopic composition of living planktonic foraminifera in the western North Atlantic. Science 207, 61–63.

Fenton, M., Geiselhart, S., Rohling, E., Hemleben, C., 2000. Aplanktonic zones in the Red Sea. Marine Micropaleontology 40, 277–294.

Filippelli, G. M., Sierro, F. J., Flores, J., Vázquez, A., Utrilla, R., Pérez-Folgado, M., Latimer, J., 2003. A sediment–nutrient–oxygen feedback responsible for productivity variations in Late Miocene sapropel sequences of the western Mediterranean. Palaeogeography, Palaeoclimatology, Palaeoecology 190, 335–348.

Grothe, A., Andreetto, F., Reichart, G.-J., Wolthers, M., Van Baak, C. G., Vasiliev, I., Stoica, M., Sangiorgi, F., Middelburg, J. J., Davies, G. R., 2020. Paratethys pacing of the Messinian Salinity Crisis: Low salinity waters contributing to gypsum precipitation? Earth and Planetary Science Letters 532, 116029.

Guido, A., Jacob, J., Gautret, P., Laggoun-Défarge, F., Mastandrea, A., Russo, F., 2007. Molecular fossils and other organic markers as palaeoenvironmental indicators of the Messinian Calcare di Base Formation: normal versus stressed marine deposition (Rossano Basin, northern Calabria, Italy). Palaeogeography, Palaeoclimatology, Palaeoecology 255, 265–283.

Gvirtzman, Z., Manzi, V., Calvo, R., Gavrieli, I., Gennari, R., Lugli, S., Reghizzi, M., Roveri, M., 2017. Intra-Messinian truncation surface in the Levant Basin explained by subaqueous dissolution. Geology 45, 915–918.

Haq, B., Gorini, C., Baur, J., Moneron, J., Rubino, J.-L., 2020. Deep Mediterranean's Messinian evaporite giant: How much salt? Global and Planetary Change 184, 103052.

Hemleben, C., Spindler, M., Anderson, O. R., 1989. Modern planktonic foraminifera, Springer Science & Business Media.

Hilgen, F., Bissoli, L., Iaccarino, S., Krijgsman, W., Meijer, R., Negri, A., Villa, G., 2000. Integrated stratigraphy and astrochronology of the Messinian GSSP at Oued Akrech (Atlantic Morocco). Earth and Planetary Science Letters 182, 237–251.

Hilgen, F., Krijgsman, W., Langereis, C., Lourens, L., Santarelli, A., Zachariasse, W., 1995. Extending the astronomical (polarity) time scale into the Miocene. Earth and Planetary Science Letters 136, 495–510.

Hilgen, F., Krijgsman, W., Wijbrans, J., 1997. Direct comparison of astronomical and $^{40}Ar/^{39}Ar$ ages of ash beds: potential implications for the age of mineral dating standards. Geophysical Research Letters 24, 2043–2046.

Hilgen, F., Kuiper, K., Krijgsman, W., Snel, E., van der Laan, E., 2007. Astronomical tuning as the basis for high resolution chronostratigraphy: the intricate history of the Messinian Salinity Crisis. Stratigraphy 4, 231–238.

Hilgen, F., Lourens, L., Dam, J. V., Beu, A., Boyes, A., Cooper, R., Krijgsman, W., Ogg, J., Piller, W., Wilson, D., 2012. The geologic time scale. Newsletters on Stratigraphy 45, 171–188.

Hilgen, F. J., Krijgsman, W., 1999. Cyclostratigraphy and astrochronology of the Tripolo diatomite formation pre-evaporite Messinian, Sicily, Italy. Terra Nova 11, 16–22.

Hsü, K. J., Ryan, W. B., Cita, M. B., 1973. Late Miocene desiccation of the Mediterranean. Nature 242, 240–244.

Kassis, D., Korres, G., 2020. Hydrography of the Eastern Mediterranean basin derived from argo floats profile data. Deep Sea Research Part II: Topical Studies in Oceanography 171, 104712.

Kouwenhoven, T., Morigi, C., Negri, A., Giunta, S., Krijgsman, W., Rouchy, J.-M., 2006. Paleoenvironmental evolution of the eastern Mediterranean during the Messinian: Constraints from integrated microfossil data of the Pissouri Basin (Cyprus). Marine Micropaleontology 60, 17–44.

Kouwenhoven, T., Seidenkrantz, M.-S., Van der Zwaan, G., 1999. Deep-water changes: the near-synchronous disappearance of a group of benthic foraminifera from the Late Miocene Mediterranean. Palaeogeography, Palaeoclimatology, Palaeoecology 152, 259–281.

Krijgsman, W., Blanc-Valleron, M.-M., Flecker, R., Hilgen, F., Kouwenhoven, T., Merle, D., Orszag-Sperber, F., Rouchy, J.-M., 2002. The onset of the Messinian salinity crisis in the Eastern Mediterranean (Pissouri Basin, Cyprus). Earth and Planetary Science Letters 194, 299–310.

Krijgsman, W., Capella, W., Simon, D., Hilgen, F. J., Kouwenhoven, T. J., Meijer, P. T., Sierro, F. J., Tulbure, M. A., van der Berg, B. C., van de Schee, M, 2018. The Gibraltar corridor: Watergate of the Messinian salinity crisis. Marine Geology 403, 238–246.

Krijgsman, W., Gaboardi, S., Hilgen, F., Iaccarino, S., Kaenel, E. d., Laan, E. v. d., 2004. Revised astrochronology for the Ain el Beida section (Atlantic Morocco): no glacio-eustatic control for the onset of the Messinian Salinity Crisis. Stratigraphy 1, 87–101.

Krijgsman, W., Hilgen, F., Langereis, C., Santarelli, A., Zachariasse, W., 1995. Late Miocene magnetostratigraphy, biostratigraphy and cyclostratigraphy in the Mediterranean. Earth and Planetary Science Letters 136, 475–494.

Krijgsman, W., Hilgen, F., Langereis, C., Zachariasse, W., 1994. The age of the Tortonian/Messinian boundary. Earth and Planetary Science Letters 121, 533–547.

Krijgsman, W., Hilgen, F., Marabini, S., Vai, G., 1999b. New paleomagnetic and cyclostratigraphic age constraints on the Messinian of the Northern Apennines (Vena del Gesso Basin, Italy). Mem. Soc. Geol. Ital 54.

Krijgsman, W., Hilgen, F., Raffi, I., Sierro, F., Wilson, D., 1999a. Chronology, causes and progression of the Messinian salinity crisis. Nature 400, 652–655.

Langereis, C., 1979. An attempt to correlate two adjacent Tortonian marine clay sections in western Crete using magnetostratigraphic methods. Bull 21, 194–214.

Lofi, J., 2018. Seismic Atlas of the Messinian Salinity Crisis markers in the Mediterranean Sea, Volume 2.

Lofi, J., Déverchère, J., Gaullier, V., Gillet, H., Gorini, C., Guennoc, P., Loncke, L., Maillard, A., Sage, F., Thinon, I., 2011a. Atlas of the "Messinian salinity crisis" seismic markers in the Mediterranean and Black seas. Commission for the Geological Map of the World (CGGMW), Mém. Soc. géol. France, ns 179, 72.

Lofi, J., Sage, F., Déverchère, J., Loncke, L., Maillard, A., Gaullier, V., Thinon, I., Gillet, H., Guennoc, P., Gorini, C., 2011b. Refining our knowledge of the Messinian salinity crisis records in the offshore domain through multi-site seismic analysis. Bulletin de la Société géologique de France 182, 163–180.

Lourens, L., Hilgen, F., Gudjonsson, L., Zachariasse, W., 1992. Late Pliocene to early Pleistocene astronomically forced sea surface productivity and temperature variations in the Mediterranean. Marine Micropaleontology 19, 49–78.

Lozar, F., Violanti, D., Bernardi, E., Dela Pierre, F., Natalicchio, M., 2018. Identifying the onset of the Messinian salinity crisis: a reassessment of the biochronostratigraphic tools (Piedmont Basin, NW Italy). Newsletters on Stratigraphy 51, 11–31.

Lugli, S., Manzi, V., Roveri, M., C. B., S., 2010. The Primary Lower Gypsum in the Mediterranean: A new facies interpretation for the first stage of the Messinian salinity crisis. Palaeogeography, Palaeoclimatology, Palaeoecology 297, 83–99.

Mancini, A. M., Gennari, R., Ziveri, P., Mortyn, P. G., Stolwijk, D. J., Lozar, F., 2020. Calcareous nannofossil and foraminiferal trace element records in the Sorbas Basin: A new piece of the Messinian Salinity Crisis onset puzzle. Palaeogeography, Palaeoclimatology, Palaeoecology, 109796.

Manzi, V., Gennari, R., Hilgen, F., Krijgsman, W., Lugli, S., Roveri, M., Sierro, F. J., 2013. Age refinement of the Messinian salinity crisis onset in the Mediterranean. Terra Nova 25, 315–322.

Marchitto, T., Curry, W., Lynch-Stieglitz, J., Bryan, S., Cobb, K., Lund, D., 2014. Improved oxygen isotope temperature calibrations for cosmopolitan benthic foraminifera. Geochimica et Cosmochimica Acta 130, 1–11.

McCaffrey, M., Lazar, B., Holland, H., 1987. The evaporation path of seawater and the coprecipitation of Br (super-) and K (super+) with halite. Journal of Sedimentary Research 57, 928–937.

McCorkle, D. C., Bernhard, J. M., Hintz, C. J., Blanks, J. K., Chandler, G. T., Shaw, T. J., 2008. The carbon and oxygen stable isotopic composition of cultured benthic foraminifera. Geological Society, London, Special Publications 303, 135–154.

Meijer, P. T., 2006. A box model of the blocked-outflow scenario for the Messinian Salinity Crisis. Earth and Planetary Science Letters 248, 486–494.

Meijer, P. T., 2012. Hydraulic theory of sea straits applied to the onset of the Messinian Salinity Crisis. Marine Geology 326, 131–139.

Murray, J., 1991. Ecology and palaeoecology of benthic foraminifera, Longman Scientific and Technical, Harlow, Essex, UK.

Negri, A., Villa, G., 2000. Calcareous nannofossil biostratigraphy, biochronology and paleoecology at the Tortonian/Messinian boundary of the Faneromeni section (Crete). Palaeogeography, Palaeoclimatology, Palaeoecology 156, 195–209.

Pierre, C., 1999. The oxygen and carbon isotope distribution in the Mediterranean water masses. Marine Geology 153, 41–55.

Ravelo, A., Fairbanks, R., Philander, S., 1990. Reconstructing tropical Atlantic hydrography using planktontic foraminifera and an ocean model. Paleoceanography 5, 409–431.

Rohling, E., Fenton, M., Jorissen, F., Bertrand, P., Ganssen, G., Caulet, J., 1998. Magnitudes of sea-level lowstands of the past 500,000 years. Nature 394, 162–165.

Rohling, E., Marino, G., Grant, K., 2015. Mediterranean climate and oceanography, and the periodic development of anoxic events (sapropels). Earth-Science Reviews 143, 62–97.

Rohling, E., Schiebel, R., Siddall, M., 2008. Controls on Messinian lower evaporite cycles in the Mediterranean. Earth and Planetary Science Letters 275, 165–171.

Rohling, E., Sprovieri, M., Cane, T., Casford, J. S., Cooke, S., Bouloubassi, I., Emeis, K., Schiebel, R., Rogerson, M., Hayes, A., 2004. Reconstructing past planktic foraminiferal habitats using stable isotope data: a case history for Mediterranean sapropel S5. Marine Micropaleontology 50, 89–123.

Rohling, E. J., Gieskes, W. W., 1989. Late Quaternary changes in Mediterranean intermediate water density and formation rate. Paleoceanography 4, 531–545.

Roveri, M., Flecker, R., Krijgsman, W., Lofi, J., Lugli, S., Manzi, V., Sierro, F. J., Bertini, A., Camerlenghi, A., De Lange, G., 2014a. The Messinian Salinity Crisis: past and future of a great challenge for marine sciences. Marine Geology 352, 25–58.

Roveri, M., Lugli, S., Manzi, V., Reghizzi, M., Rossi, F., 2020. Stratigraphic relationships between shallow-water carbonates and primary gypsum: insights from the Messinian succession of the Sorbas Basin (Betic Cordillera, Southern Spain). Sedimentary Geology 404, 105678.

Roveri, M., Manzi, V., Bergamasco, A., Falcieri, F., Gennari, R., Lugli, S., Schreiber, B., 2014b. Dense shelf water cascading and Messinian canyons: a new scenario for the Mediterranean salinity crisis. American Journal of Science 314, 751–784.

Ryan, W., 1973. Geodynamic implications of the Messinian crisis of salinity, Messinian Events in the Mediterranean. CW Drooger, 26–38, Kon. Nedl. Akad. Wetensch., Amsterdam.

Ryan, W., Hsü, K., Cita, M., Dumitrica, P., Lort, J., Maync, W., Nesteroff, W., Pautot, G., Stradner, H., Wezel, F., 1973. Leg 13. Initial Reports of the Deep Sea Drilling Project 13, 1–1447.

Sabino, M., Schefuß, E., Natalicchio, M., Pierre, F. D., Birgel, D., Bortels, D., Schnetger, B., Peckmann, J., 2020. Climatic and hydrologic variability in the northern Mediterranean across the onset of the Messinian salinity crisis. Palaeogeography, Palaeoclimatology, Palaeoecology 545, 109632.

Sachse, M., 1997. Die Makrilia-Flora (Kreta, Griechenland): Ein Beitrag zur neogenen Klima-und Vegetationsgeschichte des östlichen Mittelmeeergebietes, ETH Zurich.

Schenau, S., Antonarakou, A., Hilgen, F., Lourens, L., Nijenhuis, I., Van der Weijden, C., Zachariasse, W., 1999. Organic-rich layers in the Metochia section (Gavdos, Greece): evidence for a single mechanism of sapropel formation during the past 10 My. Marine Geology 153, 117–135.

Seidenkrantz, M.-S., Kouwenhoven, T., Jorissen, F., Shackleton, N., Van der Zwaan, G., 2000. Benthic foraminifera as indicators of changing Mediterranean–Atlantic water exchange in the late Miocene. Marine Geology 163, 387–407.

Selli, R., 1973. An outline of the Italian Messinian. In: Drooger, C. W. (Ed.), Messinian Events in the Mediterranean. Verhandelingen van de Koninklijke Nederlandse Akademie van Wetenschappen (B): North-Holland Amsterdam 76 (4), 150–171.

Shackleton, N., 1974. Attainment of isotopic equilibrium between ocean water and the benthonic foraminifera genus Uvigerina: isotopic changes in the ocean during the last glacial.

Shackleton, N., Hall, M., 1984. Oxygen and carbon isotope stratigraphy of Deep Sea Drilling Project hole 552A: Plio-Pleistocene glacial history. Init. Rep. DSDP 81, 599–609.

Shackleton, N. J., Opdyke, N. D., 1973. Oxygen isotope and palaeomagnetic stratigraphy of Equatorial Pacific core V28-238: Oxygen isotope temperatures and ice volumes on a 105 year and 106 year scale. Quaternary research 3, 39–55.

Sierro, F., Flores, J., Francés, G., Vazquez, A., Utrilla, R., Zamarreño, I., Erlenkeuser, H., Barcena, M., 2003. Orbitally-controlled oscillations in planktic communities and cyclic changes in western Mediterranean hydrography

during the Messinian. Palaeogeography, Palaeoclimatology, Palaeoecology 190, 289–316.
Sierro, F., Hilgen, F., Krijgsman, W., Flores, J., 2001. The Abad composite (SE Spain): a Messinian reference section for the Mediterranean and the APTS. Palaeogeography, Palaeoclimatology, Palaeoecology 168, 141–169.
Simon, D., Meijer, P., 2015. Dimensions of the Atlantic–Mediterranean connection that caused the Messinian Salinity Crisis. Marine Geology 364, 53–64.
Simon, D., Meijer, P. T., 2017. Salinity stratification of the Mediterranean Sea during the Messinian crisis: A first model analysis. Earth and Planetary Science Letters 479, 366–376.
Simone, L., 1980. Ooids: a review. Earth-Science Reviews 16, 319–355.
Sissingh, W., 2008. Punctuated Neogene tectonics and stratigraphy of the African-Iberian plate-boundary zone: Concurrent development of Betic-Rif basins (southern Spain, northern Morocco). Netherlands Journal of Geosciences/Geologie en Mijnbouw 87, 241–289.
Summons, R., Bird, L., Gillespie, A., Pruss, S., Roberts, M., Sessions, A., 2013. Lipid biomarkers in ooids from different locations and ages: evidence for a common bacterial flora. Geobiology 11, 420–436.
Topper, R., Meijer, P. T., 2015. The precessional phase lag of Messinian gypsum deposition in Mediterranean marginal basins. Palaeogeography, Palaeoclimatology, Palaeoecology 417, 6–16.
Tzanova, A., Herbert, T. D., Peterson, L., 2015. Cooling Mediterranean Sea surface temperatures during the Late Miocene provide a climate context for evolutionary transitions in Africa and Eurasia. Earth and Planetary Science Letters 419, 71–80.
Usiglio, M., 1849. Etudes sur la composition de l'eau de la Mediterranee et sur l'exploitation des sels qu'elle contient. Annales Chim. Phys. 3 (27), 172–191.
Van der Zwaan, G., Jorissen, F., De Stigter, H., 1990. The depth dependency of planktonic/benthic foraminiferal ratios: constraints and applications. Marine Geology 95, 1–16.
Van Hinsbergen, D., Kouwenhoven, T., Van der Zwaan, G., 2005. Paleobathymetry in the backstripping procedure: Correction for oxygenation effects on depth estimates. Palaeogeography, Palaeoclimatology, Palaeoecology 221, 245–265.
Van Hinsbergen, D. J., Meulenkamp, J. E., 2006. Neogene supradetachment basin development on Crete (Greece) during exhumation of the South Aegean core complex. Basin Research 18, 103–124.
Zachariasse, W., 1979. Planktonic Foraminifera from section Potamida I: Taxonomic and phyletic aspects of keeled globorotaliids and some paleoenvironmental estimates. Utrecht Micropaleontological Bulletin 21, 129–166.
Zachariasse, W., van Hinsbergen, D., Fortuin, A., 2008. Mass wasting and uplift on Crete and Karpathos during the early Pliocene related to initiation of south Aegean left-lateral, strike-slip tectonics. Geological Society of America Bulletin 120, 976–993.
Zachariasse, W. J., van Hinsbergen, D. J., Fortuin, A. R., 2011. Formation and fragmentation of a late Miocene supradetachment basin in central Crete: implications for exhumation mechanisms of high-pressure rocks in the Aegean forearc. Basin Research 23, 678–701.

Manuscript received: March 15, 2021
Revisions required: July 20, 2021
Revised version received: September 08, 2021
Manuscript accepted: September 09, 2021

The pdf version of this paper includes an electronic supplement

Please save the electronic supplement contained in this pdf-file by clicking the blue frame above. After saving rename the file extension to .zip (for security reasons Adobe does not allow to embed .exe, .zip, .rar etc. files).

Table of contents – Electronic Supplementary Material (ESM)